Title: Dysregulation of macrophage lipid metabolism underlies intracellular bacterial neuroinvasion

Authors: Zhou Sha[1, #], Kun Yang[2, #], Shoupeng Fu[3, #], Xiaoyong Tong[4, #], Hui Yang[1], Huiling Fang[1], Qianqian He[1], Ning Li[5, 6], Xinyu Shu[5, 6], Qi Liu[1], Yongliang Du[1], Beibei Fu[1], Yan Xiong[1], Dong Guo[1], Jin Liu[4], Qian Li[7], Hao Zeng[8], Xiaokai Zhang[8], Rui Yao[9], Xushuo Zhang[10], Wenjin Guo[3], Xuhu Mao[7], Mian Long[5, 6], Xiaoyuan Lin[7, 11, *], Quanming Zou[8, *], Haibo Wu[1, *]

1 School of Life Sciences, Chongqing University, Chongqing 401331, China

2 Chongqing Public Health Medical Center, Chongqing 400036, China

3 School of Veterinary Medicine, Jilin University, Changchun 130062, China

4 School of Pharmaceutical Sciences, Chongqing University, Chongqing 401331, China

5 Center of Biomechanics and Bioengineering, Key Laboratory of Microgravity (National Microgravity Laboratory), and Beijing Key Laboratory of Engineered Construction and Mechanobiology, Institute of Mechanics, Chinese Academy of Sciences, Beijing 100190, China

6 School of Engineering Sciences, University of Chinese Academy of Sciences, Beijing 100049, China

7 Department of Clinical Microbiology and Immunology, College of Pharmacy and Laboratory Medicine, Army Medical University (Third Military Medical University),

Chongqing 400038, China.

8 National Engineering Research Center of Immunological, Department of Microbiology and Biochemical Pharmacy, College of Pharmacy and Laboratory Medicine, Army Medical University (Third Military Medical University), Chongqing 400038, China.

9 Department of Pathology, Chongqing Hygeia Hospital, Chongqing 401331, China

10 Zhejiang Toyouvax Biopharming, Hangzhou 311100, China

11 Institut für Virologie, Freie Universität Berlin, Robert-von-Ostertag-Str. 7-13, Berlin 14163, Germany.

# Equally Contributing Authors

* Corresponding authors

Xiaoyuan Lin, linxiaoyuan23@163.com

Quanming Zou, qmzou2007@163.com

Haibo Wu, hbwu023@cqu.edu.cn

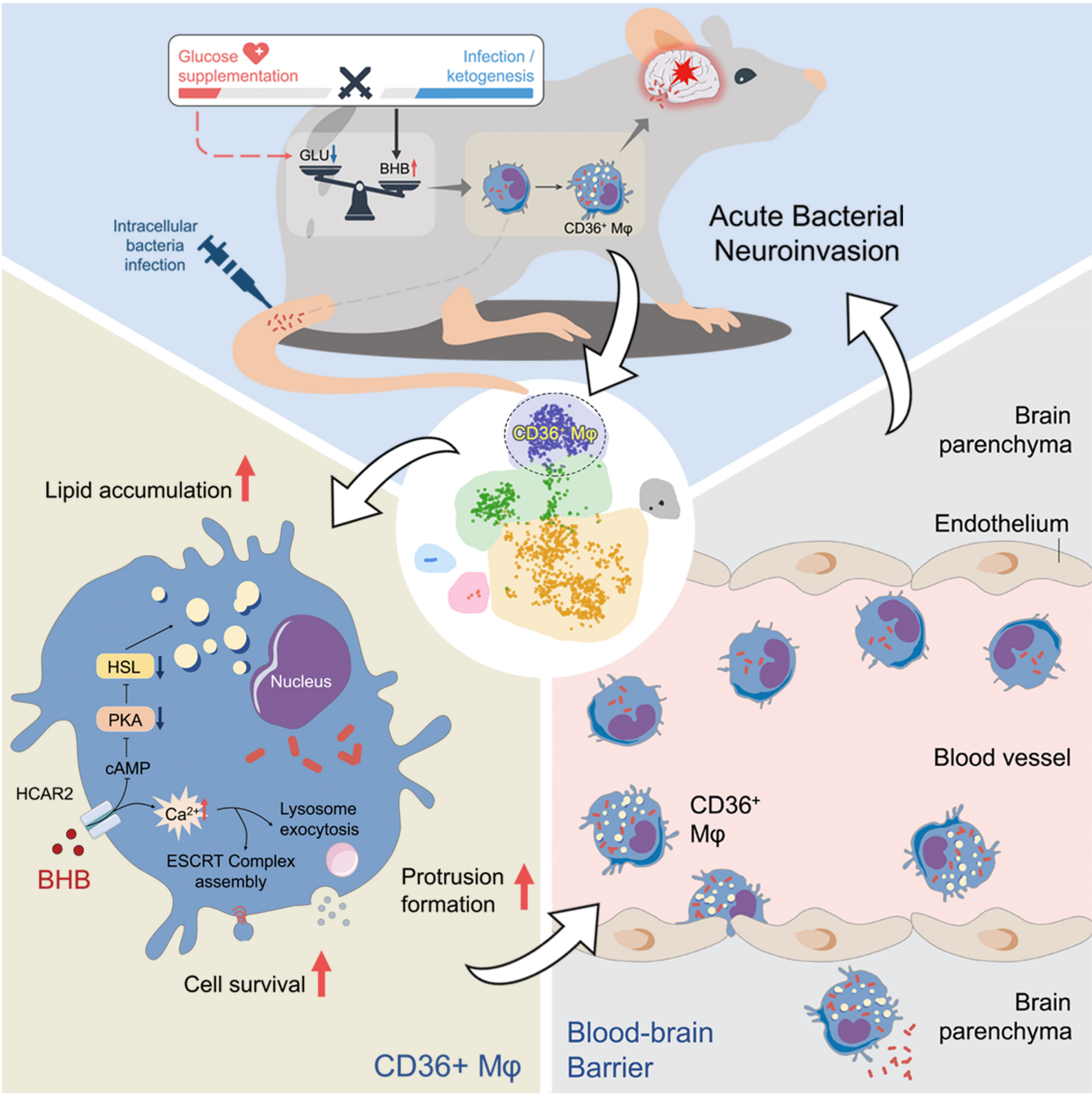

Graphic abstract

Summary

Acute infection of the central nervous system is one of the deadliest diseases, but the mechanisms by which intracellular bacteria infiltrate the brain remain poorly understood. Phagocytic cells are usually recognized as the battlefield on which war is waged against intracellular bacteria; however, little is known about how the intracellular bacteria take advantage of infected phagocytes to access the brain. In this study, we find that a novel $CD36^+$ $Fabp4^+$ $Pparg^+$ macrophage subpopulation ($CD36^+$ macrophage) participates in penetration of the brain by intracellular bacteria without disruption of the brain-blood barrier. Biomechanical analysis reveals that abundant protrusions and adhesion molecules on $CD36^+$ macrophages confer significant resistance to the mechanical stress of blood flow, thereby providing more opportunities for these macrophages to adhere to the vascular endothelial surface. Through metabolomics analysis, we find that macrophage lipid metabolism is dysregulated during bacterial neuroinvasion, and that β-hydroxybutyrate promotes the formation and survival of $CD36^+$ macrophages. Importantly, ketogenesis exacerbates symptoms during bacterial neuroinvasion, which could be alleviated by supplementing with physiological level of glucose. Taken together, our findings uncover a pathway by which intracellular bacteria hijack macrophages to invade the brain, suggesting that lipid metabolism might play a role in the prevention or resolution of bacterial neuroinvasion.

Keywords: intracellular bacteria; neuroinvasion; $CD36^+$ macrophage; ketogenesis; β-hydroxybutyrate

Highlights

1. Intracellular bacteria hijack $CD36^+$ Mφ for brain invasion without disruption of BBB.
2. $CD36^+$ Mφ has enhanced adhesion to CVECs and increased resistance to shear flow.
3. Ketogenesis promotes bacterial neuroinvasion that can be halted by glucose treatment.
4. Serum β-hydroxybutyrate and $CD36^+$ Mφ accumulation fuel bacterial meningitis in human.

Introduction

Meningitis is an inflammation of the protective membranes covering the brain that caused by pathogen infection.[1,2] As a life-threatening infection with an extremely high mortality rate, acute bacterial meningitis usually occurs secondary to infected organs. The blood-brain barrier (BBB) is the foremost line of defense, which consists of brain endothelial cells working in concert with pericytes, smooth muscle cells, astrocytes, microglia and macrophages to protect the central nervous system from infections.[3] Currently, pathogens in the bloodstream are thought to penetrate the BBB via three

main pathways: transcellular entry, paracellular entry or so-called “Trojan horse” spread.[4] It is known that some bacteria can invade the brain directly by accumulating during transcytosis or disrupting the tight junction, accompanied by BBB leakage. For example, *Streptococcus pneumoniae* (*S. pneumoniae*) interacts with host receptors on endothelial cell monolayers to achieve brain invasion by transcytosis.[5-7] *Neisseria meningitidis* hijacks specific host-pathogen interactions to redistribute the tight junction or adhesion proteins, leading to BBB disruption.[8] However, the route of “Trojan horse” spread by which bacteria circumvent without damaging the BBB has rarely been reported. Some intracellular bacteria, including *Listeria monocytogenes* (*L. monocytogenes*) and *Mycobacterium tuberculosis* (*M. tuberculosis*), can invade the brain tissue with the assistance of host cells, [9,10] but the underlying mechanisms remain unclear. Efforts to understand the factors that promote the neuroinvasion of intracellular bacteria and host responses to these pathogens are urgently needed.

Phagocytes, such as neutrophils and macrophages, play dominant roles in host response to intracellular bacteria.[11] The primary function of phagocytes is to uptake and destroy microorganisms and cell debris through tissue circulation and migration. [12,13] Via phagocytosis and antigen presentation, phagocytes act rapidly as the first line of defense against bacterial infections. However, intracellular bacteria can employ sophisticated strategies to replicate within phagocytes and evade host immune surveillance.[14-16] Recently, Marc Lecuit et al. showed that the surface protein internalin B of *L. monocytogenes* protects infected monocytes from immune killing

by $CD8^+$ T cells, thus prolonging the lifespan of infected cells and facilitating the spread of infection throughout the central nervous system.[16] In this context, phagocytes, especially monocytes and macrophages, might play important roles during neuroinvasion, but exactly how intracellular bacteria take advantage of infected macrophages is not well understood.

The metabolism of host immune cells is reprogrammed during infection. Metabolic signaling helps awaken the immune cells to resist pathogenic invasion. For example, glycolysis bolsters T cell immunity to prevent *L. monocytogenes* infection.[17] In addition, many studies have shown that bacteria can actively or passively manipulate host metabolites to evade clearance by the host immune system. [14,18,19] *Legionella pneumophila* induces Warburg-like metabolism by secreting the type 4 secretion system effector MitF and decreases oxidative phosphorylation (OXPHOS) in infected macrophages to increase the pathogen's likelihood of survival.[18] A recent report indicates that $Nav1.8^+$ nociceptors send signals to meningeal macrophages via the calcitonin gene-related peptide, and this neuroimmune axis suppresses host defenses and exacerbates bacterial meningitis.[19] These findings imply a potentially close connection between host metabolism and bacterial brain invasion.

Ketogenesis, induced by fasting or dietary supplementation, is a metabolic pathway that provides an alternative form of energy for the body and is closely related to host immune response. [20,21] A recent study reports that in pneumonia caused by

Pseudomonas aeruginosa, ketone bodies are recycled to the lungs via OXPHOS to maintain airway homeostasis. [22] Consistently, a ketogenic diet is reported to promotes T cell responses in pulmonary viral infections.[23,24] However, researchers have also found that pathogens can achieve intracellular survival and infection progression by manipulating host ketogenesis.[25] Mice fed a ketogenic diet develop a hyperinflammatory response to systemic lipopolysaccharide and an increased mortality rate, phenomena that are independent of diet-induced microbiota and hyperglycemia.[25] Therefore, the role of ketogenesis in the progression and migration of infections is controversial.[26] β-hydroxybutyrate (BHB) produced by ketogenesis is well known to promote the accumulation of intracellular lipid bodies, which serve as both a source of nutrients and a secure niche for intracellular bacteria.[27] However, how ketogenesis and BHB participate in regulating monocytic/macrophagic homeostasis and their roles in bacterial neuroinvasion are poorly defined.

In this study, we discovered a novel subpopulation of $CD36^+$ macrophages that served as immune " Trojan horses" that crosses but does not destroy the BBB, enabling intracellular bacterial neuroinvasion. This macrophage subset has a foamy-like phenotype, which improves the cells' ability to stay and migrate vertically on the cerebrovascular endothelial surface under the mechanical stress of blood flow. Furthermore, we found that serum BHB, which might be produced by a ketogenic diet, exacerbated bacterial neuroinvasion by increasing the formation and promoting the survival of $CD36^+$ macrophages in peripheral blood. More importantly, we

demonstrated that the perturbation of lipid metabolism during bacterial brain invasion could be rectified by supplementing mice with physiological level of glucose, thereby suppressing the generation of $CD36^+$ macrophages and greatly attenuating the clinical symptoms of meningitis. Our study outlines a new common strategy employed by intracellular bacteria in brain invasion, which could be a potential therapeutic target in the treatment of bacterial meningitis.

Results

$CD36^+$ macrophages are potential carriers of bacteria during brain invasion

To study the role of immune cells in bacterial neuroinvasion, we constructed an acute meningitis mice model of infection, and found that at 24 hours post infection, *L. monocytogenes* massively invaded the brain and the mice began to die (Figure S1A and S1B). Evans blue staining showed that no extravasation of dye in the whole brain, indicating no disruption of BBB in this acute meningitis model (Figure S1C and S1D). Then, peripheral blood mononuclear cells (PBMCs) were collected and single-cell RNA-sequencing (scRNA-seq) was performed (Figure 1A). Immune cell lineages were identified using canonical surface markers of dendritic cells (DCs: *Xcr1, Flt3, CD209a*), NK cells (*Nkg7*), T cells (*CD3*), monocyte/macrophages (Mo/Mφ: *Fcgr1, Adgre1*), B cells (*CD79*), neutrophils (*S100a9, S100a8*; Figure 1B and 1C).[28] Among these lineages, Mo/Mφ are involved in phagocytosis and intracellular killing of microorganisms; however, intracellular bacteria can also live in these cells to achieve long-term latent infection.[29] In this case, Mo/Mφ (n=3535 cells) were extracted and

reclustered *in silico* to precisely delineate subpopulations and their distributions before and after neuroinvasion. Based on differentially expressed cell surface markers and transcripts, we annotated Mo/Mφ into 6 subpopulations (Figure 1D, S1E). Results showed that the percentage of Cluster 2 cells was sharply increased in the neurolisteriosis group (Figure S1F). Further, we found that Cluster 2 cells expressed high levels of genes related to lipid accumulation, including *CD36*, peroxisome proliferator–activated receptor gamma (*Pparg*), fatty-acid binding protein 4 (*Fabp4*), *CD9*, apolipoprotein E epsilon (*ApoE*), and triggering receptor expressed on myeloid cells 2 (*Trem2*; Figure. 1E).[30-34] These data implied that the functional role of Cluster 2 ($CD36^+$) macrophages was closely related to lipid metabolism.

To understand the characteristics of Cluster 2 macrophages, $CD36^+$ and $CD36^-$ macrophages were isolated from peripheral blood by fluorescence-activated cell sorting. Compared with $CD36^-$ macrophages, the $CD36^+$ subpopulation exhibited significantly higher granularity (SSC^{hi}; Figure S1G), which indicated the number of proteins or organelles they contained and the protrusions on their surfaces. The sorted macrophages were cultured *in vitro* overnight and then labeled with BODIPY FL, a lipophilic probe for polar and neutral lipids. Results showed that the $CD36^+$ subpopulation accumulated significantly more lipid droplets than the $CD36^-$ macrophages (Figure S1H). We also performed Oil Red O staining to validate this finding (Figure S1H). To confirm the lipid uptake ability of the $CD36^+$ macrophages, we used fluorescently labeled 1,1′-dioctadecyl-3,3,3′,3′-tetramethylindocarbocyanine

198 perchlorate (Dil)–conjugated oxidized low-density lipoprotein (oxLDL) particles and
199 our finding showed that $CD36^+$ macrophages took up more than twice as much ox-
200 LDL as $CD36^-$ macrophages (Figure S1H). These data indicated that lipid metabolism
201 in Cluster 2 macrophages was dysregulated during brain invasion.
202
203 Next, we performed flow cytometry to detect percentage changes in $CD36^+$
204 macrophages over time during neurolisteriosis (Figure S1I). The results showed that
205 the percentage of $CD36^+$ macrophages in peripheral blood steadily increased over
206 time during neuroinvasion (Figure 1F). The $CD36^+$ subgroup could exceed 52% of all
207 macrophages (Figure 1G). In addition, the percentage of $CD36^+$ macrophages in
208 peripheral blood were positively associated with bacterial load in the brain (Figure
209 1H). These data implied that $CD36^+$ macrophages might be involved in bacterial
210 neuroinvasion. Furthermore, immunofluorescence co-localization analysis was used
211 to validate this hypothesis. The results showed that the number of $CD36^+$
212 macrophages attached to cerebrovascular endothelial cells (CVECs) increased as
213 neuroinvasion progressed in the acute meningitis model (Figure 1I). Taken together,
214 these results suggested that $CD36^+$ macrophage might play an important role in
215 bacterial brain invasion.
216
217 **$CD36^+$ macrophages facilitate transport of intracellular bacteria across the**
218 **blood-brain barrier**
219 Next, we sought to understand how necessary $CD36^+$ macrophages were to bacterial

neuroinvasion. Using mouse primary CVECs and neurons in a Transwell system, we constructed an *in vitro* BBB model (Figure 2A). Ox-LDL has been reported to induce a foamy-like phenotype by enhancing CD36 expression[35]; therefore, we converted peritoneal macrophages isolated from mice into $CD36^+$ macrophages by treating them with different concentrations of ox-LDL for 24 hours (Figure S2A). Subsequently, macrophages were infected with *L. monocytogenes* (MOI=10) and then inoculated in the upper Transwell chamber of the BBB model. We confirmed that intracellular bacterial load increased with the transformation of peritoneal macrophages into $CD36^+$ macrophages (Figure S2B). Of note, the assistance of ox-LDL–stimulated macrophages significantly increased the number of *L. monocytogenes* organisms crossing the BBB in a dose-dependent manner (Figure 2B). Using crystal violet staining, we also demonstrated a dose-dependent increase in the number of macrophages penetrating the endothelial monolayer upon stimulation with ox-LDL (Figure 2C and 2D).

To understand whether the increase in $CD36^+$ macrophages favored the transfer of *L. monocytogenes* into the brain *in vivo*, we performed adoptive macrophage transfer experiments through tail vein injection based on a cyclophosphamide (CTX)-induced immunosuppressive mouse model (Figure 2E). Consistent with previous studies, *L. monocytogene*-induced clinical phenotype and mortality were relieved in the mice transferred with purified peritoneal macrophages ($CD36^+$ Mφ group; Figure 2F, S2C and S2D).[36,37] However, body weight was reduced, comprehensive clinical scoring was

increased, and survival time was shortened in the mice transferred with $CD36^+$ macrophages compared with the control ($CD36^+$ Mφ group; Figure 2F, S2C and S2D). Furthermore, we showed that brain bacterial loads in mice transferred with $CD36^+$ macrophages were significantly higher than those in mice transferred with purified peritoneal macrophages (Figure 2G). Interestingly, bacterial loads did not differ among the lung, spleen, and liver (Figure S2E). We also tested proinflammatory factor levels in plasma and brain homogenate. The results showed that levels of interleukin 6 (IL-6) and tumor necrosis factor alpha (TNF-α) were remarkably increased (Figure 2H and 2I), indicating a more severe phenotype of meningitis in the $CD36^+$ macrophage transferred group. However, brains of mice transferred with $CD36^+$ macrophages exhibited no Evans blue extravasation, suggesting that these macrophages facilitated the transfer of *L. monocytogenes* into the brain without disrupting the BBB (Figure S2F and S2G). Pathological histology analysis confirmed the existence of more severe inflammation and neuronal damage in the cerebral cortices in mice transferred with $CD36^+$ macrophages than in those of control (Figure S2F and S2H). In addition, when mice were infected with a relatively low dose (5×10^7 CFU/mouse) of *L. monocytogenes*, the difference in bacterial load in brain tissues between $CD36^+$ macrophage transferred mice and the control group was even greater than that under high dose condition (Figure S2I and S2J). These data suggested that neuroinvasion mediated by $CD36^+$ macrophages were not restricted to an acute meningitis model induced by high dose bacteria.

We then wondered whether $CD36^+$ macrophages might play the same role during brain invasion by other intracellular bacteria. In the relevant experiment, a positive correlation between $CD36^+$ macrophages and neuroinvasion was observed in meningitis models of the intracellular bacterium *Salmonella typhimurium* (*S. typhimurium*; Figure S3A and S3B). We observed the same result in neuroinvasion model of Methicillin-resistant *Staphylococcus aureus* (MRSA; Figure S3C and S3D), which, although not a classical intracellular pathogen, exhibits significant intracellular habitation.[38] However, this finding was not validated in a neuroinvasion model of the extracellular bacterium *S. pneumoniae* (Figure S3E and S3F). Next, we performed adoptive macrophage transfer experiments to further verify the carrier role of $CD36^+$ macrophages in intracellular bacterial invasion of the brain. We again observed differences in brain tissue bacterial loads between the $CD36^+$ macrophage transferred and control groups in the meningitis models of MRSA (Fig. S3G-S3K), but not in models using *S. pneumoniae* (Figure S3L-S3O). Taken together, these data suggested that $CD36^+$ macrophages greatly contributed to the process of intracellular bacterial neuroinvasion.

Proprotein convertase subtilisin/kexin 9 (PCSK9) belongs to the proprotein convertase family, whose members participate in cholesterol and fatty acid (FA) metabolism. [39,40] Intracellular low-density lipoprotein cholesterol (LDL-C) accumulates because LDL receptor located on the cell membrane cannot be degraded normally in $PCSK9^{-/-}$ mice.[41,42] We found that PCSK9-deficient macrophages had

286 significantly higher lipid content compared with control (Figure S4A and S4B) and
287 that more *L. monocytogene* organisms parasitized PCSK9$^{-/-}$ macrophages than they
288 parasitized wild-type (WT) cells (Figure S4C). During neurolisteriosis, PCSK9$^{-/-}$ mice
289 had higher percentages of CD36^{+} macrophages in peritoneal blood than their
290 littermates (Figure S4D). Therefore, we used PCSK9$^{-/-}$ mice as a model of
291 spontaneously forming CD36^{+} macrophages, and verified the reliability of our
292 findings through adoptive macrophages transfer. After recovery from transfer for 12
293 hours, recipient mice were intraperitoneally injected with 2×10^{8} CFU of *L.*
294 *monocytogenes*; 12 h later, samples were collected for further examinations (Figure
295 2J). We found that brain bacterial loads were significantly higher in PCSK9$^{+/+}$
296 recipients that had been transferred with PCSK9$^{-/-}$ macrophages than in those that had
297 received WT macrophages (Figure 2K). Similar results were observed in the PCSK9$^{-/-}$
298 recipients (Figure 2K). However, differences in bacterial load manifested in brain
299 tissues only, not in other organs such as the lung, spleen, and liver (Figure S4E).
300 Consistently, the mortality rate, and pro-inflammatory factors in the plasma and brain
301 homogenate were aggravated in both PCSK9$^{+/+}$ and PCSK9$^{-/-}$ recipients by transfer of
302 PCSK9$^{-/-}$ macrophages (Figure 2L, S4F and S4G). Since *L. monocytogene* is a
303 foodborne pathogen that can invade the body through the gastrointestinal tract, we
304 further confirmed the above-mentioned finding by oral administration of *L.*
305 *monocytogenes* in the same experimental model (Figure 2M and 2N, S4H-S4J). Taken
306 together, these data indicated that excessive lipid accumulation contributed to the
307 formation of CD36^{+} macrophages, thereby facilitating neuroinvasion by intracellular

308 bacteria.

309

310 **Shear flow analysis demonstrates increased adhesion and resistance of CD36$^+$**

311 **macrophages during neuroinvasion**

312 We next asked how CD36$^+$ macrophages exploited their properties to accumulate on

313 the cerebral blood vessel wall and participate in the process of intracellular bacterial

314 neuroinvasion. Using a two-dimensional live-cell flow chamber assay with a

315 microfluidic chip [43], we deciphered the multistep process of how macrophages

316 adhered to and moved on the surface of vascular endothelium under physiological

317 flow (Figure 3A). Cellular adhesion ability was calculated by counting total

318 macrophages adhering to the endothelial monolayer under a given shear stress. We

319 found that as the percentage of CD36$^+$ macrophages increased, so did the number of

320 cells adhering to the endothelial monolayer (Figure 3B and 3C). Because adherent

321 cells could be detached by an increase in shear stress, we tested the dynamics of

322 CD36$^+$ macrophages' shear resistance. The results showed that such resistance was

323 significantly stronger than that of control macrophages: CD36$^+$ macrophages

324 outstandingly resisted high shear stress (Figure 3D). Further, we investigated the

325 effect of endothelial density on macrophagic adhesion. Results showed that

326 endothelial cell density, rather than cell type, greatly affected macrophagic adhesion,

327 and CD36$^+$ macrophages tended to adhere to the surface of dense endothelial cells

328 (Figure S5A-S5D).

329

330 Once attached to the endothelial monolayer, the macrophage crawls along it and finds
331 a place to cross it in the presence of blood flow. [44,45] We next tested the performance of
332 $CD36^+$ macrophages in post-arrest crawling on the endothelial monolayer. We
333 acquired sequential images of macrophages at a shear stress of 2 dyn/cm^2 and then
334 analyzed them by defining various parameters of crawling dynamics (Figure S5E).
335 The observations were presented by crawling trajectories of each individual cells
336 (Figure 3E), and we found that the crawling ability of adherent $CD36^+$ macrophages
337 was dampened, reflecting in shortened crawling displacement and slower crawling
338 speed (Figure 3F and 3G). However, we saw no obvious differences in crawling
339 duration (Figure S5F). Directionality is also a critical aspect of cell crawling
340 dynamics, it is quantified as the ratio of displacement along shear flow to the
341 perpendicular. Our results showed that the directionality of macrophages was slightly
342 but significantly enhanced by ox-LDL stimulation, implying that macrophagic
343 foaminess tended to drive cell crawling in the vertical direction (Figure 3H). We also
344 compared a key dynamic parameter of transmigration duration, which is defined as
345 the interval from the timepoint of cell arrival at the site to the endpoint of completion
346 of transmigration beneath the endothelial monolayer (Figure S5G). The result showed
347 that transmigration duration was significantly shortened in $CD36^+$ macrophage
348 (Figure 3I).
349
350 Considering that protrusion is critical for cell crawling and migration, we then
351 investigated whether intercellular lipid could affect the formation of protrusions. The

352 results showed that the numbers, as well as the lengths of protrusions were
353 significantly increased in $CD36^+$ macrophages (Figure 3J and 3K). We further
354 quantified macrophagic cell area and found that the mean area of $CD36^+$ macrophages
355 was significantly larger than the control (Figure 3L). Additionally, we examined
356 various integrins and adhesive ligands expressed on the cell surface, which have been
357 reported to be involved in adhesion and migration.[46] The results showed that the
358 expression levels of α-integrins, β-integrins and intercellular adhesion molecules were
359 significantly upregulated in the infected $CD36^+$ macrophages (Figure 3M).
360 Collectively, these data suggested that the foaminess of macrophages greatly
361 enhanced their ability to adhere under mechanical stress, predisposing them to stay
362 and to migrate vertically on the surface of CVECs; this might be attributable to the
363 formation of protrusions as well as the expression of integrins and adhesion ligands.
364

365 **β-hydroxybutyrate promotes $CD36^+$ macrophage formation and exacerbates**
366 **neuroinvasion**

367 Next, we performed lipid metabolomics analysis of serum samples to reveal how
368 $CD36^+$ macrophages were formed during bacterial neuroinvasion. Principal
369 component analysis (PCA) showed that distinct metabolite genotype clusters were
370 generated in the neurolisteriosis group (Figure 4A). The volcano plot indicated that 70
371 FAs were upregulated and 71 FAs were downregulated ($p < 0.05$, $|\log_2(\text{fold change})|$
372 > 1) in the neurolisteriosis group (Figure 4B, Table S1). The 70 upregulated FAs
373 were classified into four subclusters by the number of carbon atoms in the alkyl chain.

We found thatβ-hydroxybutyrate (BHB), which has been reported to favor the foamy-like phenotype of macrophages [47], was the only short-chain FA among all upregulated FAs (Figure 4C). Kyoto Encyclopedia of Genes and Genomes (KEGG)-based analysis revealed that metabolites related to the synthesis and degradation of ketone bodies were enriched (Figure S6A), and metabolomics data showed that BHB was significantly increased during neuroinvasion (Figure S6B). Further, we found that BHB levels in mice serum climbed steadily over time in the acute meningitis model of *L. monocytogenes* infection (Figure 4D).

Then, we sought to explore the reason of enhanced ketogenesis during the brain invasion. Liver tissues of acute meningitis mice model were collected for transcriptome analysis by RNA-sequencing (RNA-seq). The results showed that compared with control group, the genes associated with ketogenesis were sharply upregulated in the liver of mice suffered from neurolisteriosis, while these genes were moderately increased in the mild infection group (Figure S6C). KEGG-based analysis and gene-set enrichment analysis (GSEA) among the neurolisteriosis and control group revealed that the differentially expressed (DE) genes were enriched in glycolysis or gluconeogenesis (Figure S6D and S6E). To validate this finding, we measured the serum glucose levels of mice and found that glucose levels significantly decreased and remained low during the *L. monocytogene*-induced neuroinvasion (Figure S6F); meanwhile, we observed a significant decrease in cellular energy and an increase in ADP/ATP ratios in mice with neurolisteriosis compared to the control

group (Figure S6G and S6H). These data implied that the decrease in glucose level and increase in ketogenesis may be induced by excessive glycolysis during *L. monocytogene*-induced neuroinvasion. Further, we showed that the extracellular acidification rates (ECAR) were significantly increased in the livers of mice with neurolisteriosis (Figure S6I). This data was confirmed by the measurement of lactate, which is the end product of glycolysis (Figure S6J). Also, we found that mice experienced weight loss and reduced food intake, which to a certain extent contributed to the enhancement of ketogenesis after infection (Figure S6K and S6L). Interestingly, there was no significant difference in these indicators between the mild infection group and the control group during the experiments (Figure S6F-S6L). Furthermore, a steady increase of serum BHB and decrease of glucose level was also observed in the meningitis models established using *S. typhimurium* and MRSA (Figure S6M and S6N). These data indicated that production of BHB was significantly induced during bacterial neuroinvasion, and it was probably due to the low serum glucose level induced by excessive glycolysis.

As previously reported, autocrine or paracrine BHB directly activates macrophages function mainly via the hydroxycarboxylic acid receptor 2 (HCAR2).[27] Therefore, we next used HCAR2 knockout mice to study whether BHB could promote bacterial neuroinvasion. We confirmed that lipid accumulation and percentage of $CD36^{+}$ macrophages all increased dramatically upon BHB stimulation, and there was no significant difference when HCAR2 was knocked out (Figure 4E-4G). BHB inhibits

adenylyl cyclase activity through the HCAR2 receptor and reduces cellular cyclic adenosine monophosphate (cAMP) levels, thereby protecting lipid droplets from lipolysis by hormone-sensitive lipases (HSL).[27] As a result, we found that cAMP pretreatment eliminated the decrease in HSL activity, the increase in lipid content and intercellular bacterial burden stimulated by BHB; however, this phenomenon was not found in HCAR2-deficient macrophages (Figure S6O-S6Q). By using the *in vitro* BBB model (Figure 2A), the number of bacteria crossing the barrier increased significantly in response to BHB stimulation in controls, but not in HCAR2$^{-/-}$ macrophages (Figure 4H). Next, peritoneal macrophages from HCAR2$^{+/+}$ and HCAR2$^{-/-}$ mice were isolated to further assess the effects of BHB on the biophysical dynamics of macrophages. The data demonstrated that BHB significantly altered the static or shear-resistant adhesion of control macrophages, but not of HCAR2$^{-/-}$ macrophages (Figure 4I-4K). We also found that BHB greatly impaired the crawling ability, including shortened crawling displacement, slowed down crawling speed and unpredictable directionality of macrophages (Figure 4L-4O). In addition, the transmigratory ability of macrophages was significantly increased when cells were pretreated with BHB (Figure 4P). Consistently, the expression levels of the α-integrin family were significantly upregulated by BHB treatment in controls, but not in HCAR2-deficient macrophages (Figure 4Q). Taken together, these data indicated that BHB facilitated the formation of CD36^{+} macrophages through the HCAR2 receptor, thereby affecting the process of bacterial neuroinvasion.

BHB promotes the survival of macrophages via HCAR2-mediated calcium influx

Because the foamy stage appears to be a terminal point of macrophage differentiation [48], we wondered whether, in addition to converting peritoneal macrophages to the foamy phenotype, cell survival also contributed to the increase in absolute quantity of $CD36^+$ macrophages induced by BHB treatment. The results showed that the lactate dehydrogenase (LDH) activity in the culture medium was significantly reduced in response to BHB treatment, indicating a decrease in cell death (Figure 5A). Propidium iodide (PI) staining was used to evaluate the membrane integrity of infected macrophages, and we found that the proportion of PI^+ cells decreased from 59.7% to 24.5% under BHB stimulation, with no significant difference in cell viability between the BHB treatment and control groups when HCAR2 was knocked out (Figure 5B and 5C). Calcium influx is generally recognized as a signal that triggers cell membrane repair.[49] To investigate the impact of BHB-HCAR2 signaling on cytosolic calcium concentration, infected macrophages were loaded with Fluo-4 AM, a fluorescent Ca^{2+} indicator. The results showed that BHB induced remarkable accumulation of intracellular calcium, and HCAR2 knockdown eliminated calcium influx in macrophages (Figure 5D). Pretreatment of macrophages with BAPTA, a Ca^{2+} chelator, reversed the BHB-induced increase in cell survival (Figure 5E and 5F). Further, we tested whether calcium flux was associated with $CD36^+$ macrophage-mediated intracellular bacterial penetration of the BBB. As a result, inhibition of calcium flux had no effect on bacterial uptake by macrophages in the upper chamber (Figure S7A); however, we observed differences in bacterial loads in the macrophages

462 that had crossed the barrier (Figure 5G).

463

464 We next investigated how BHB maintained the survival of $CD36^+$ macrophages. As
465 previously reported, calcium influx initiates membrane repair mainly through
466 recruitment of the endosomal sorting complexes required for transport (ESCRT)
467 machinery.[50] Our data showed that BHB treatment significantly increased the number
468 of puncta that were positive for charged multivesicular body protein 4B (CHMP4B),
469 which indicated assembly of ESCRT in the infected macrophages; HCAR2
470 knockdown or BAPTA treatment could block this membrane repair process (Figure
471 5H and 5I, S7B and S7C).Cellular membrane repair also relies on lysosomes, which
472 can rapidly fuse with the plasma membrane when intracellular Ca^{2+} concentration
473 rises. Therefore, we examined lysosomal exocytosis in the infected macrophages
474 using exofacial lysosomal-associated membrane protein 1 (LAMP1) and the release of
475 lysosomal enzymes, such as acid phosphatase (ACP), β-galactosidase (β-gal) and β-
476 hexosaminidase (β-hex). The results confirmed that BHB promoted the lysosomal
477 exocytosis in infected macrophages through the HCAR2 receptor (Figure 5J-5L, S6D-
478 S6F). These data collectively indicated that BHB signaling activated Ca^{2+}-mediated
479 membrane repair, thereby maintaining the survival of $CD36^+$ macrophages via the
480 HCAR2 receptor.

481

482 **Ketogenesis exacerbates intracellular bacterial neuroinvasion**

483 BHB can be synthesized via the metabolism of FAs and ketogenesis.[51] To understand

484 the relationship between ketogenesis and bacterial meningitis, we gave mice different
485 doses of ketone ester drink for 4 weeks, and then infected them with *L.*
486 *monocytogenes* via intraperitoneal injection (Figure 6A). The data showed that ketone
487 ester elevated the levels of serum BHB and the proportion of $CD36^{+}$ macrophages in
488 peritoneal blood (Figure 6B and S8A), accompanied by remarkable increases in the
489 clinical scores, mortality rate and bacterial load in brain tissues (Figure 6C and 6D,
490 S8B). Dietary modulation can increase and maintain circulating metabolites in human
491 circulation, and a growing amount of evidence demonstrates that a ketogenic diet
492 elevates BHB levels.[52] The ketogenic diet is a low-carb, high-fat diet that causes
493 weight loss and provides numerous health benefits, including alleviating symptoms of
494 neurodegenerative diseases, cardiovascular diseases, and cancers.[21,53-55] We next asked
495 whether a ketogenic diet was associated with neurolisteriosis. $HCAR2^{-/-}$ mice and
496 their littermates were fed a normal or ketogenic diet for 4 weeks respectively, and
497 then infected with *L. monocytogenes* by intraperitoneally injection (Figure 6E). As a
498 result, the lifespan of $HCAR2^{+/+}$ mice fed a ketogenic diet was significantly shortened
499 under *L. monocytogenes* infection, and the survival disadvantage caused by dietary
500 modulation was abrogated by HCAR2 knockout (Figure 6F). Consistently, the clinical
501 scores (Figure. S8C), percentages of $CD36^{+}$ macrophages in peritoneal blood (Figure
502 6G), the intracellular bacterial burden of macrophages (Figure 6H), and bacterial
503 loads in brain tissue (Figure 6I) were all greatly increased in $HCAR2^{+/+}$ mice on a
504 ketogenic diet. Interestingly, mice in this group lost less weight than mice in the
505 control group, and experienced greater spread of bacteria to other organs (Figure 6I

and S8D). We then examined the levels of pro-inflammatory factors in the plasma and brain homogenate. The results showed that a ketogenic diet significantly increased the levels of pro-inflammatory cytokines and induced more severe neuronal damage in HCAR2$^{+/+}$ mice, while it had no effect on HCAR2$^{-/-}$ mice (Figure 6J-6M). Notably, Evans blue extravasation was not detected in the brain of mice fed a ketogenic diet, ruling out the possibility of direct damage to the BBB (Figure 6L and S8E). These data were confirmed by oral administration of *L. monocytogenes* in the same experimental model (Figure S8F-S8I). We also used MRSA to further verify our findings. The data indicated that, as expected, the ketogenic diet promoted brain invasion by MRSA and exacerbated symptoms of meningitis (Figure S8J-S8L). Taken together, our data showed that a ketogenic diet could exacerbate bacterial neuroinvasion and hasten the demise of mice, primarily depending on the elevation in serum BHB via the HCAR2 receptor.

Our data thus far suggested that BHB played an important role in bacterial neuroinvasion in mice, and the enhancement in ketogenesis was probably induced by the low serum glucose level. We then evaluated the effects of restoring blood glucose level on the outcomes of infected mice. The results showed that under the acute meningitis model of *L. monocytogenes* infection, supplementing mice with glucose every 12 hours to restore blood glucose levels resulted in a significant decrease in BHB levels and CD36^{+} macrophages percentages (Figure S9A-S9D). Surprisingly, we showed that four rounds of glucose supplementation significantly improved the

survival rate of mice, reduced their brain bacterial burden and pro-inflammatory cytokines levels (Figure S9E-S9I). These data indicated that glucose homeostasis restricted the brain invasion of *L. monocytogenes* infection and alleviated meningitis symptoms in mice.

Serum BHB fuels the symptoms of human bacterial meningitis

A retrospective study that based on the Medical Information Mart for Intensive Care IV (MIMIC-IV) was performed to explore the risk factors of bacterial meningitis in human. As a result, ferritin (OR 5.09, 95% CI 1.55-16.71), fibrinogen (OR 3.57, 95% CI 1.13-11.25), LDL (OR 3.31, 95% CI 1.01-10.83), glucose (OR 2.17, 95% CI 1.04-4.50) and aspartate amino transferase (OR 2.16, 95% CI 1.01-4.63) were identified as independent risk factors, whereas potassium (OR 0.42, 95% CI 0.20-0.87), alkaline phosphatase (AP, OR 0.38, 95% CI 0.18-0.83), phosphate (OR 0.23, 95% CI 0.11-0.50), high-density lipoprotein (HDL, OR 0.19, 95% CI 0.05-0.66) and transferrin (OR 0.14, 95% CI 0.04-0.50) were identified as protective factors for patients with bacterial meningitis (Figure S10A). Next, we asked whether the accumulation of $CD36^{+}$ macrophages or BHB could also be identified and were associated with bacterial meningitis in human clinical samples. Gender- and age-matched bacterial meningitis subjects and healthy individuals were recruited and peripheral blood samples were collected for analysis (Figure 7A). Since blood glucose is a risk factor for meningitis and BHB level can be dramatically affected by glycolysis, subjects with abnormal blood glucose or insulin concentrations were excluded from the two

550 groups (Figure S10B-S10E). As a result, serum BHB levels were significantly
551 elevated in meningitis patients compared with healthy controls, suggesting an
552 infection-induced ketogenesis (Figure 7B). Interestingly, serum cholesterol levels,
553 including total cholesterol (TC) and LDL-C were increased in meningitis patients
554 compared with healthy controls, while HDL-C was slightly but not significant
555 reduced (Figure S10F-10H). This finding was consistent with data from our
556 retrospective study based on MIMIC-IV (Figure S10A). To investigate whether BHB
557 was associated the severity of infection, we further divided patients into three groups,
558 high BHB (in the top 1/3 among samples tested, n=21), moderate (middle 1/3, n=20)
559 and low (bottom 1/3, n=21; Figure 7A). Clearly, patients with high BHB levels
560 exhibited higher clinical scores than patients with low BHB levels (Figure 7C).
561 Consistently, high-BHB patients had higher cell counts and more protein in the
562 cerebrospinal fluid (CSF; Figure 7D and 7E); higher infection indices such as white
563 blood cell counts (WBC; Figure 7F) and procalcitonin (PCT; Figure 7G); and higher
564 values for markers of inflammatory conditions such as erythrocyte sedimentation rate
565 (ESR; Figure 7H) and C-reactive protein (CRP; Figure 7I), suggesting increased
566 disease severity. These data implied that infection-induced ketogenesis might provide
567 important fuel for severe bacterial neuroinvasion.
568
569 To explore the dynamics of $CD36^+$ macrophages and BHB in the pathogenesis of
570 bacterial meningitis, we followed-up with 7 individuals during their hospitalization.
571 We found that $CD36^+$ macrophages and BHB levels in patients tended to increase

572 during disease progression, and decrease during the recovery stage (Figure 7J and
573 7K). To further confirm the relationship between $CD36^+$ macrophages and bacterial
574 meningitis pathology, we collected PBMCs from patients or healthy controls for
575 analysis. Compared with healthy controls, the expression levels of genes involved in
576 cholesterol uptake were significantly increased, while those of genes related to
577 cholesterol utilization and excretion were decreased in macrophages from meningitis
578 patients (Figure 7L). Taken together, these data indicated that BHB fueled human
579 bacterial meningitis by promoting the development of $CD36^+$ macrophages.
580

581 **Discussion**

582 Our findings suggested that $CD36^+$ macrophage might serve as a carrier for
583 intracellular bacteria that colonize in the brain, facilitating the penetration of these
584 bacteria across the BBB. Generally, the BBB prevents pathogens from crossing unless
585 there is significant trauma to the brain. However, specific bacteria can break through
586 the BBB via their unique mechanisms and cause severe brain infections.[1,16]. In this
587 study, we discovered that intracellular bacteria may prefer to exploit a "Trojan horse"
588 pathway, which causes little scathe to the BBB but enables acute brain invasion.
589 $CD36^+$ macrophages could be hijacked by intracellular bacteria and serve as vehicles
590 for neuroinvasion. Compared with peritoneal macrophages, $CD36^+$ macrophages tend
591 to have more protrusions and greater cell area, which make them more conducive to
592 colonization on CVECs under the pressure of blood flow. Based on the above-
593 mentioned remarkable characteristics, $CD36^+$ macrophages have the potential to

594 become carriers of engineered intracellular bacteria for bacteriotherapy.

595

596 Pathogens can exploit most of the host's nutrients, including glycerol, FAs, and
597 several other carbon substances, to reprogram immune cells.[56] Our findings
598 demonstrated that intracellular bacteria can actively influence host free FA
599 metabolism (Figure 4A-4C) and reprogram macrophages, thereby exacerbating
600 neuroinvasion. The foamy-like phenotype of macrophages is formed through
601 dysregulation of lipid metabolism, and it impairs the immune function of
602 macrophages and contributes to pathogenesis. For example, foamy macrophage
603 necrosis was previously reported to expand tuberculous lesions in lung parenchyma,
604 causing progressive destruction of lung tissue and loss of lung function in patients
605 with active disease.[57] In this study, we discovered that BHB produced by a ketogenic
606 diet promoted the formation of a foamy-like phenotype in $CD36^+$ macrophages in
607 peripheral blood, thereby facilitating bacterial neuroinvasion. Interestingly, we found
608 that serum cholesterol levels, including TC and LDL-C were significantly higher in
609 meningitis patients than in healthy controls (Figure S10F and S10H). We hypothesize
610 that cholesterol or other lipid metabolites might also contribute to the formation of
611 $CD36^+$ macrophages. However, this hypothesis should be further verified
612 experimentally.

613

614 Our biomechanical data indicated that $CD36^+$ macrophages adhered more strongly to
615 the endothelial surface than normal macrophages, and that this adhesion-enhancing

effect was more pronounced when endothelial cells were dense (Figure 3B and 3C, S5A and S5B). This suggested that $CD36^+$ macrophage-mediated bacterial invasion affected the brain to a greater extent than other tissues. Accordingly, we showed that the increase in $CD36^+$ macrophages in peripheral blood led to the transfer of bacteria mainly to the brain, rather than to other organs (Figure 2G and S2E). However, we found that a ketogenic diet and ketone ester supplementation significantly increased bacterial load not only in the brain, but also in other tissues such as the liver and lung (Figure 6D and 6I). This suggested that ketogenesis, in addition to promoting the generation of $CD36^+$ macrophage, might play other unknown roles in the intracellular bacterial infections. Therefore, the role of ketogenesis in the formation of $CD36^+$ macrophages and the contribution of ketogenesis to bacterial neuroinvasion should be further determined.

The host's basal nutritional status may also greatly influence the outcome of infection. A recent study reported that glucose supplementation in mice has a protective effect against *Yersinia pseudotuberculosis* infection.[58] Our results indicated that the decrease in blood glucose level and enhancement of ketogenesis in the liver may be induced by excessive glycolysis during bacterial neuroinvasion (Figure S6C-S6I). Interestingly, we found that mice experienced weight loss and decreased appetite during the bacterial meningitis, and the two events occurred almost simultaneously (Figure S6K and S6L). These data together imply that maintenance of normal blood sugar levels may be critical for the development, progression, and prognosis of meningitis.

Therefore, we attempted to restore the blood sugar levels of acute meningitis mice by intraperitoneal injection of glucose, and surprisingly we found that glucose supplementation significantly alleviated the clinical symptoms of meningitis, reduced bacterial burden in the brain and improved the survival rate of mice (Figure S9). These findings indicate that in addition to antibacterial therapy, nutritional therapy plays a vital role in the clinical treatment of bacterial meningitis.

Overall, this study demonstrated that a BHB-rich environment created by the ketogenic diet rendered mice more susceptible to *L. monocytogene*-induced neuroinvasion. Mechanistically, BHB protected $CD36^+$ macrophages from senescence via HCAR2-mediated membrane repair. However, inhibition of HCAR2 signaling or calcium influx reversed the improvement in $CD36^+$ macrophage survival but did not completely reverse the exacerbation in bacterial neuroinvasion induced by BHB (Figure 5E-5G). These data suggested that BHB-induced bacterial brain invasion was not solely dependent on HCAR2 signaling but that other potential mechanisms might also be involved in this process. However, this hypothesis requires further experimental verification.

Acknowledgments

This work was supported by the National Natural Science Foundation of China (No. 92369115), the Fundamental Research Funds for the Central Universities (No. 2023CDJXY-009 and 2019CDYGZD009), Natural Science Foundation of Chongqing,

China (No. CSTB2023NSCQMSX0402), and Chongqing Talents: Exceptional Young Talents Project (No. cstc2021ycjh-bgzxm0099). The funders had no role in study design, data collection and analysis, decision to publish, or preparation of the manuscript.

Author Contributions

H.W., Q.Z., X.L. and Z.S. conceived and designed the study. Z.S., H.Y., H.F., Q.H., B.F., Y.X. and D.G. performed the animal experiments. Z.S., K.Y., Q.H., Q.L., Y.D. and Xushuo Z. carried out healthy volunteer and patient recruitment and sample collection. Z.S., N.L. and X.S. carried out the live-cell flow chamber assays. H.W., Z.S., K.Y., H.Y. and Xiaokai Z. collected and analyzed the data. X.T., S.F., J. L., R.Y., W.G., X.M. and M.L. contributed to experimental material and insightful suggestions. H.W., X.L., Xushuo Z. and Z.S. wrote the manuscript. H.W. and Q.Z. coordinated the project. All authors read and approved the final manuscript.

Declaration of interests

The authors declare no competing interests.

Figure Legends

Figure 1. Identification of CD36^{+} macrophage accumulation during neurolisteriosis.

682 (A) Summary of experimental design (n=5 control mice and n=7 mice infected with
683 2×10^8 CFU *L. monocytogenes* for 24 hours).
684 (B) Uniform Manifold Approximation and Projection (UMAP) representation of
685 integrated transcriptome-based clustering. A total of 17351 peripheral blood
686 mononuclear cells (PBMCs) were clustered and major immune cell lineages were
687 identified.
688 (C) Dot plot showing the expression of selected transcripts in immune cell clusters.
689 All transcripts were significantly enriched in the pertinent clusters with adjusted $p <$
690 0.05.
691 (D) A t-distributed Stochastic Neighbor Embedding (tSNE) analysis of the re-
692 clustered cells corresponding to monocytes and macrophages (baseline, n=1804;
693 neurolisteriosis, n=1731).
694 (E) Expression of the indicated transcripts (encoding genes associated with lipid
695 accumulation) was projected onto a monocyte/macrophage tSNE plot.
696 (F-G) An acute mouse neurolisteriosis model was generated by intraperitoneal
697 injection of 2×10^8 CFU *L. monocytogenes.* Quantification of $CD36^+$ macrophages in
698 PBMCs (F) and total macrophages (G) was detected by flow cytometry (n=5 for each
699 group). Experiments were performed in duplicate. Data are presented as mean ± SEM.
700 $*p < 0.05$, $**p < 0.01$.
701 (H) Correlation between $CD36^+$ macrophages and bacterial burdens in brain during
702 the neurolisteriosis. R, correlation coefficient.
703 (I) Immunofluorescence staining of $CD36^+$ macrophages in cerebral vasculature of

mice with neurolisteriosis. $CD36^+$ macrophages were stained with CD11b (red) and CD36 (green). The boundary of vascular was depicted in dashed lines. Scale bar, 100 μm.

Abbreviations: PBMC, peripheral blood mononuclear cell; i.p., intraperitoneally; CFU, colony forming units.

Figure 2. Infected $CD36^+$ macrophages transfer bacteria into brain parenchyma *in vitro* and *in vivo*.

(A) Schematic diagram of an *in vitro* BBB model based on Transwell system.

(B) Quantification of bacterial burden in the macrophages penetrating into the lower chamber of Transwell system under different concentrations of ox-LDL.

(C-D) (C) Representative image of macrophages that penetrated into the lower chamber. Scale bar, 100 μm. (D) Quantification of the penetrating cells in each field of view.

(E) Experimental diagram of adoptive macrophage transfer.

(F-I) After the adoptive macrophage transfer, recipient mice were intraperitoneally infected with 2×10^8 CFU *L. monocytogenes*. (F) Survival of recipient mice (n=10 for each group). (G-I) Bacterial burdens in brains (G), and cytokine levels in plasma (H) and brain homogenate (I) of recipient mice on day 1.25 (n=5 for each group).

(J-N) (J) Schematic diagram of adoptive macrophage transfer and infection experiments among $PCSK9^{+/+}$ (WT) and $PCSK9^{-/-}$ (KO) mice. Peritoneal macrophages from $PCSK9^{+/+}$ and $PCSK9^{-/-}$ mice were injected into $PCSK9^{+/+}$ and

PCSK9$^{-/-}$ mice, respectively, followed by *L. monocytogenes* infection.

(K, M) Bacterial burdens in the brains of recipient mice after intraperitoneal injection (K) or oral administration (M) of *L. monocytogenes* (n=5 for each group).

(L, N) Survival of recipient mice after intraperitoneal injection (L) or oral administration (N) of *L. monocytogenes* (n=10 for each group).

Experiments were performed in duplicate (E-N) or triplicate (A-D). Data are presented as mean ± SEM. *$p < 0.05$, **$p < 0.01$. Abbreviations: ox-LDL, oxidized low density lipoprotein; FOV, field of view; NS, normal saline; PMφ, purified peritoneal macrophages; CD36^{+} Mφ, CD36^{+} macrophages; i.p., intraperitoneally; ns, nonsignificant.

Figure. 3 Two-dimensional live-cell flow chamber assay of the migration characteristics of infected CD36^{+} macrophages.

(A) Schematic diagram of live-cell flow chamber experiment. Primary peritoneal macrophages were pretreated with ox-LDL for 24 hours and then infected with *L. monocytogenes* (MOI=10) for 6 hours.

(B-C) (B) Optical images of ox-LDL pretreated macrophages adhering to the surface of monolayer endothelial cells under shear flow. Scale bar, 200 μm. (C) Quantification of adherent cells in each field of view.

(D) Resistance to shear flow after adhesion of ox-LDL pretreated macrophages to endothelial cells. Upon 10-min adherence of equal macrophages to the monolayer endothelial cells at 1 dyn/cm^{2}, the shear stress was stepwise increased to 2, 4, 8, 16,

and 32 dyn/cm^2 for 30 s sequentially to detach those adhered cells.

(E-H) Crawling dynamics of ox-LDL pretreated macrophages under shear flow. (E) Typical trajectories of ox-LDL pretreated macrophages crawling on monolayer endothelial cells. For each trajectory, the arrested sites of macrophages were overlaid at the origin of the diagram (x/y=0/0) and the corresponding end points were indicated with dots. Arrows indicate the flow direction. (F-H) Quantification of crawling displacement (F), velocity (G) and directness (H).

(I) Transmigration duration of ox-LDL pretreated macrophages after adhesion to the surface of monolayer endothelial cells.

(J-K) Quantification of the number (J) and mean length (K) of protrusions in ox-LDL pretreated macrophages.

(L) Quantification of cell area in ox-LDL pretreated macrophages.

(M) qRT-PCR analysis of relative expression of genes associated with intercellular adhesion molecules.

Experiments were performed in triplicate. Data are presented as mean ± SEM. *$p < 0.05$, **$p < 0.01$. Abbreviations: ox-LDL, oxidized low density lipoprotein.

Figure 4. β-hydroxybutyrate aggravates bacterial neuroinvasion by promoting the formation of CD36$^+$ macrophages via HCAR2 receptor.

(A-C) Lipid metabolomic profiling analyses of serum from the mice with or without neurolisteriosis. The mice of neurolisteriosis group were infected with 2×10^8 CFU *L. monocytogenes* for 24 hours (n=6 for each group). (A) Principal coordinates analysis

(PCA) analysis of differences between groups. (B) Expression of fatty acids (FAs) in the serum was shown in the volcano plot. Differentially expressed FAs were selected with |log2 fold change|>1 and adjusted $P < 0.05$. The dark blue dots represent down-regulated FAs and the orange dots represent up-regulated FAs. (C) Classification of the up-regulated FAs (SCFA, short chain fatty acids; MCFA, medium chain fatty acids; LCFA, long chain fatty acids; VLCFA, very long chain fatty acids) shown in the pie chart.

(D) Biochemical analysis of serum BHB levels in mice during the neurolisteriosis.

(E-Q) Primary peritoneal macrophages were extracted from 8-week-old $HCAR2^{+/+}$ and $HCAR2^{-/-}$ mice in preparation for further functional analysis. $HCAR2^{+/+}$ and $HCAR2^{-/-}$ macrophages were pretreated with BHB (10 mM) for 24 hours and then infected with *L. monocytogenes* (MOI=10) for 6 hours.

(E-F) (E) Flow cytometry analysis of BODYPY FL 493/503 in BHB-treated macrophages (0, 5, 10 mM). (F) The histogram represents normalized MFI.

(G) Flow cytometry analysis of $CD36^{+}$ macrophages in BHB-treated macrophages (0, 5, 10 mM).

(H) Quantification of bacterial burden in the macrophages penetrating into the lower chamber of Transwell system. The macrophages stimulated with ox-LDL (80 ng/ml) were used as positive control.

(I-J) (I) Optical images of adherent macrophages on the surface of monolayer endothelial cells. Scale bar, 200 μm. (J) Quantification of adherent cells in each field of view.

(K) Resistance to shear flow after adhesion of macrophages to endothelial cells.

(L-P) Crawling and migrating dynamics of infected macrophages under shear flow.

(L) Typical trajectories of infected macrophages crawling on monolayer endothelial cells. Quantification of crawling displacement (M), velocity (N), directness (O) and transmigration duration (P).

(Q) mRNA expression of intercellular α-integrin in infected macrophages.

Experiments were performed in duplicate (D) or triplicate (E-Q). Data are presented as mean ± SEM. *$p < 0.05$, **$p < 0.01$. Abbreviations: ns, nonsignificant; BHB, β-hydroxybutyrate; MFI, mean value of fluorescence intensity.

Figure 5. β-hydroxybutyrate promotes the survival of macrophage via HCAR2-mediated calcium influx.

(A-L) Primary peritoneal macrophages were extracted from 8-week-old $HCAR2^{+/+}$ and $HCAR2^{-/-}$ mice, cells were then infected with *L. monocytogenes* (MOI=10) for 6 hours.

(A-C) $HCAR2^{+/+}$ and $HCAR2^{-/-}$ macrophages were pretreated with BHB (10 mM) before infection. (A) Quantification of the percentage of released lactate dehydrogenase (LDH) in cell culture medium. (B) Immunofluorescence of Propylene glycol (PI)-stained macrophages. DAPI (blue) labels the nucleus and PI (red) labels the cell membrane. (C) Quantification of the percentage of PI^{+} cells after infection.

(D) Flow cytometry analysis of dynamics in intracellular calcium concentration. Infected macrophages were preloaded with Fluo-4 AM. BHB (10 mM) was added to

814 the buffer after a span of 30 s.

815 (E-G) Macrophages were pretreated with BHB (10 mM) or BAPTA (10 mM) for 24

816 hours before infection. (E) Quantification of the percentage of released lactate

817 dehydrogenase (LDH) in cell culture medium. (F) Quantification of the percentage of

818 PI^+ cells after infection. (G) Quantification of bacterial burden in the macrophages

819 penetrating into the lower chamber of Transwell system.

820 (H-I) (H) Infected macrophages were treated with BHB (10 mM). Time-lapse images

821 of CHMP4B-EGFP in macrophages were collected at 0, 5, 10, 15, 20, 30 min post

822 BHB treatment with confocal microscopy. (I) Quantification of CHMP4B-EGFP

823 puncta.

824 (J-L) $HCAR2^{+/+}$ and $HCAR2^{-/-}$ macrophages were pretreated with BHB (10 mM) for

825 24 hours before infection. (J) Flow cytometry analysis of LAMP1 expression on the

826 cell surface. (K) The histogram representing normalized MFI. (L) Quantification of

827 the lysosomal enzyme (acid phosphatase [ACP], β-galactosidase [β-gal] and β-

828 hexosaminidase [β-hex]) activity released into the culture medium.

829 Experiments were performed in triplicate. Data are presented as mean ± SEM. *$p <$

830 0.05, **$p < 0.01$. Abbreviations: ns, nonsignificant; BHB, β-hydroxybutyrate.

831

832 **Figure 6. Ketogenesis exacerbates neurolisteriosis through β-hydroxybutyrate-**

833 **HCAR2 signaling.**

834 (A-D) (A) Schematic diagram of *in vivo* KE supplementation. C57BL/6 mice were

835 supplemented with KE (10, 20 mg/ml) in drinking water for 2 weeks and then

challenged with 2×10^8 CFU *L. monocytogenes*. Serum BHB levels (B) and bacterial burdens in the parenchymal organs (D) were detected (n=5 for each group). (C) Survival of mice exposed *L. monocytogenes* (n=10 for each group).

(E-M) (E) Schematic diagram of *in vivo* ketogenic diet. $HCAR2^{+/+}$ and $HCAR2^{-/-}$ mice were treated with ketogenic or control diets, respectively, for 4 weeks, followed by intraperitoneal infection with 2×10^8 CFU *L. monocytogenes*. (F) Survival of mice exposed to *L. monocytogenes* (n=10 for each group). (G) Flow cytometry analysis of $CD36^+$ macrophages before and after neurolisteriosis. (H-M) (H-I) Bacterial burdens in peripheral blood macrophages (H) and parenchymal organs (I) of mice on day 29. (J-K) Cytokine levels in the plasma (J) and brain homogenate (K). (L) Representative images of Evans blue leakage of mouse brains and Hematein & Eosin staining of cerebral cortex tissue. (M) Pathology scores. Scale bar, 10 μm. (n=5 for each group). Experiments were performed in duplicate. Data are presented as mean ± SEM. *$p < 0.05$, **$p < 0.01$. Abbreviations: ns, nonsignificant; KE, Ketone ester; CD, control diet; KD, ketogenic diet; i.p., intraperitoneally.

Figure 7. Levels of β-hydroxybutyrate are decreased in bacterial meningitis in humans, which correlated with the severity of disease.

(A) Schematic diagram of HC (n=60) and BM (n=62) samples. The BM patients were divided into three groups according to serum BHB levels.

(B) Serum BHB level in HC and BM patients.

(C-I) Clinical scores (C), cell counts (D) and protein levels (E) in cerebrospinal fluid,

white blood cells (WBC, F), procalcitonin (PCT, G), erythrocyte sedimentation rate (ESR, H) and C-reactive protein (CRP, I) in BM patients with different BHB levels.

(J-K) Dynamics of $CD36^+$ macrophages (J) and serum BHB (K) in 7 BM donors after admission. The time after admission was divided into symptomatic and convalescent periods according to clinical and laboratory indexes of infection. The scatter plot on the right panel represents the statistics of AUC.

(L) Relative expression of genes involved in lipid metabolism in PBMCs from HC and BM patients was detected by qRT-PCR.

Data are presented as mean ± SEM. *$p < 0.05$, **$p < 0.01$. Abbreviations: ns, nonsignificant; HC, healthy control; BM, bacterial meningitis; AUC, area under the curve; BHB, β-hydroxybutyrate .

Figure S1. Additional results of identification of $CD36^+$ macrophage accumulation during the neurolisteriosis, related to Figure 1.

(A-B) C57BL/6 mice were intraperitoneally infected with 2×10^8 CFU *L. monocytogenes.* (A) Bacterial burdens in brains. (B) Survival of the mice (n=10 for each group). The yellow shading represents the range of confidence interval.

(C-D) Evans blue assay of the mouse challenged with *L. monocytogene*s (2×10^8 CFU/mouse) or LPS (2 mg/mouse). Representative images (C) and quantification of Evans blue leakage in the mouse brains (D).

(E) Cell clusters identified in 10× scRNA-seq dataset. The top 10 enriched genes for each cluster are highlighted. Normalized z-score is used to illustrate gene expression.

(F) Proportion of each cluster according to experimental conditions in Figure 1D.

(G) Gating strategy for analysis of $CD36^+$ macrophages in PBMCs.

(H) $CD36^+$ and $CD36^-$ macrophages were sorted from peripheral blood by flow cytometry and then stained with BODIPY FL 493/503 and oil Red O. Scale bar, 10 μm.

(I) Normalized intake of Dil-oxLDL by $CD36^+$ and $CD36^-$ macrophages.

Experiments were performed in duplicate (A-D) or triplicate (H-I). Data are presented as mean ± SEM. *$p < 0.05$, **$p < 0.01$.

Figure S2. Additional results of adoptive transfer of $CD36^+$ macrophages *in vitro* and *in vivo*, related to Figure 2.

(A) Conversion of mice peritoneal macrophages into $CD36^+$ macrophages by treating them with different concentrations of ox-LDL for 24 hours.

(B) Intracellular bacterial burden was quantified in macrophages challenged with *L. monocytogenes* (MOI=10) in the upper chamber of Transwell system under different concentrations of ox-LDL.

(C-H) The adoptive macrophage transfer experiment was shown in Figure 2E-2I (n=5 for each group). Recipient mice were intraperitoneally infected with 2×10^8 CFU *L. monocytogenes*. (C-D) Body weight changes (C) and clinical scores (D) of recipient mice during neurolisteriosis. (E) Bacterial burdens in other tissues (lung, spleen, liver) of recipient mice on day 1.25. (F-H) (F) Representative images of Evans blue leakage of mouse brains and Hematein & Eosin staining of cerebral cortex tissue.

Quantification of extravasation (G) and (H) pathology scores. Scale bar, 20 μm.

(J-K) After adoptive macrophage transfer, recipient mice were intraperitoneally infected with 5×10^7 CFU *L. monocytogenes*. Bacterial burdens in brains (J) and other tissues (K) of recipient mice on day 1.25 were detected.

Experiments were performed in duplicate (C-J) or triplicate (A-B). Data are presented as mean ± SEM. *$p < 0.05$, **$p < 0.01$. Abbreviations: ns, nonsignificant; NS, normal saline; PMφ, purified peritoneal macrophages; $CD36^+$ Mφ, $CD36^+$ macrophages; i.p., intraperitoneally.

Figure S3. Accumulation of $CD36^+$ macrophages exacerbate intracellular bacteria neuroinvasion.

(A-F) Mice were intravenously infected with *S. Typhimurium* (A-B), MRSA (C-D) or *S. pneumoniae* (E-F), respectively (n=5 for each group). (A, C, E) Flow cytometry analysis of $CD36^+$ macrophages during neuroinvasion. (B, D, F) Correlation between $CD36^+$ macrophages and bacterial burden in the brain during bacteria neuroinvasion. R, correlation coefficient.

(G-K) After the adoptive macrophage transfer, recipient mice were intraperitoneally infected with 2×10^8 CFU MRSA. (G) Survival of recipient mice (n=10 for each group). (H-I) Bacterial burdens in the brains (H) and other tissues (lung, spleen, liver). (J-K) Cytokine levels in plasma (J) and brain homogenate (K) of recipient mice on day 1.5 (n=5 for each group).

(L-O) Mice were intraperitoneally infected with 1×10^8 CFU *S. pneumoniae* (n=5 for

each group). (L) Survival rate of mice (n=10). (M) Bacterial burdens in tissues. (N-O) Cytokine levels in plasma (N) and brain homogenate (O) of recipient mice on day 2 (n=5 for each group).

Experiments were performed in duplicate. Data are presented as mean ± SEM. *$p < 0.05$, **$p < 0.01$. Abbreviations: ns, nonsignificant.

Figure S4. Additional results of bidirectional transfer of macrophages from PCSK9$^{+/+}$ and PCSK9$^{-/-}$ mice, related to Figure 2.

(A-B) (A) Flow cytometry analysis of lipid droplets in peritoneal macrophages of PCSK9$^{+/+}$ and PCSK9$^{-/-}$ mice. (B) The histogram represents normalized MFI.

(C) Peritoneal macrophages of PCSK9$^{+/+}$ and PCSK9$^{-/-}$ mice were infected with *L. monocytogenes* (MOI=10) for 2 hours and then incubated in a fresh solution containing 5 μg/mL lysostaphin for 2 or 12 hours. Intracellular bacterial burden of infected macrophages was quantified

(D) Flow cytometry analysis of CD36^{+} macrophages during neurolisteriosis in PCSK9$^{+/+}$ and PCSK9$^{-/-}$ mice, respectively (n=5 for each group).

(E-G) Recipient mice in Figure 2J were intraperitoneally infected with 2×10^{8} CFU *L. monocytogenes*. (E) Bacterial burdens in other tissues (lung, spleen, liver). (F-G) Cytokine levels in plasma (F) and brain homogenate (G) (n=5 for each group).

(H-J) Recipient mice in Figure 2J were orally infected with 2×10^{8} CFU *L. monocytogenes*. (H) Bacterial burdens in other tissues (lung, spleen, liver). (I-J) Cytokine levels in plasma (I) and brain homogenate (J) (n=5 for each group).

Experiments were performed in duplicate (D-J) or triplicate (A-C). Data are presented as mean ± SEM. *p < 0.05, **p < 0.01. Abbreviations: ns, nonsignificant; i.p., intraperitoneally.

Figure S5. Supplemental data for the live-cell flow chamber assays, related to Figure 3.

(A-D) Optical images of *L. monocytogenes* infected macrophages (with or without ox-LDL stimulation) on the surface of endothelial monolayers with different densities (A) or endothelial monolayers derived from different tissues (C). Scale bar, 200 μm.

(B, D) Quantification of adherent cells in each field of view.

(E) Schematic trajectory used for defining macrophage crawling parameters.

(F) Crawling duration of *L. monocytogene*-infected macrophages after adhesion to endothelial monolayer surface.

(G) Relative fluorescence intensity of a macrophage on endothelial surface over time. It is a random example to illustrate the definition of transmigration duration. A 70% decrease in fluorescence intensity after a macrophage crosses a monolayer is considered successful transmigration.

Experiments were performed in triplicate. Data are presented as mean ± SEM. *p < 0.05, **p < 0.01. Abbreviations: CVEC, cerebrovascular endothelial cell; PVEC, pulmonary vascular endothelial cell; LSEC, liver sinusoidal endothelial cell; TEM, transendothelial migration; ns, nonsignificant.

Figure S6. Additional results from the influence of β-hydroxybutyrate on macrophages during neuroinvasion, related to Figure 4.

(A) KEGG enrichment analysis of lipid metabolites.

(B) Mass spectrometry analysis of serum BHB levels.

(C-E) Transcriptomics analysis of liver tissues from mice (n=3 for each group). The mice of mild infection group were infected with 2×10^6 CFU *L. monocytogenes* for 24 hours while those of neurolisteriosis group were 2×10^8 CFU. (C) Heatmap of differentially expressed (DE) genes related to ketogenesis. (D) Top20 KEGG enrichment analysis of function of DE genes between neurolisteriosis group and baseline group. (E) Gene-set enrichment analysis of glycolysis/gluconeogenesis between neurolisteriosis group and baseline group.

(F) Biochemical analysis of serum glucose levels in mice during the *L. monocytogenes* infection.

(G-J) Levels of ATP generation, (G) ratio of ADP/ATP (H), seahorse analysis of the ECAR (I) and relative abundances of lactate (J) in the liver tissues from mice with or without *L. monocytogenes* infection for 24 hours.

(K-L) Body weight changes (K) and food uptake (L) were monitored every 6 hours during neuroinvasion.

(M-N) Biochemical analysis of serum BHB and glucose levels in mice during neuroinvasion by *S. typhimurium* (M) and MRSA (N).

(O-Q) $HCAR2^{+/+}$ and $HCAR2^{-/-}$ macrophages were pretreated with BHB (10 mM) and cAMP (1 mM) for 24 hours and then infected with *L. monocytogenes* (MOI=10) for 6

hours. Quantification of the HSL activity (O), normalized MFI of BODIPY FL 493/503 (P) and the bacterial burden in the macrophages penetrating into the lower chamber of Transwell system (Q).

Experiments were performed in duplicate (F-N) or triplicate (O-Q). Data are presented as mean ± SEM. *p < 0.05, **p < 0.01. Abbreviations: BL, baseline; NL, neurolisteriosis; ns, nonsignificant; MFI, mean fluorescence intensity; HSL, hormone-sensitive lipase.

Figure S7. Additional results on the role of β-hydroxybutyrate in regulating macrophage survival, related to Figure 5.

(A-F) Primary peritoneal macrophages were extracted and then infected with *L. monocytogenes* (MOI=10) for 6 hours.

(A) Macrophages were pretreated with BHB (10 mM) or BAPTA (10 mM) for 24 hours before infection. Intracellular bacterial burden of macrophages in the upper chamber of Transwell system was quantified.

(B-C) (B) Infected macrophages were treated with BHB (10 mM). Time-lapse images of CHMP4B-EGFP in macrophages were collected at 0, 5, 10, 15, 20, 30 min post BHB treatment with confocal microscopy. (C) Quantification of CHMP4B-EGFP puncta.

(D-F) Peritoneal macrophages were pretreated with BHB (10 mM) or BAPTA (10 mM) for 24 hours before infection. (D) Flow cytometry analysis of LAMP1 expression on the cell surface. (E) The histogram representing normalized MFI. (F)

Quantification of the lysosomal enzyme activity released into the culture medium. Experiments were performed in triplicate. Data are presented as mean ± SEM. *$p < 0.05$, **$p < 0.01$. Abbreviations: ns, nonsignificant; BHB, β-hydroxybutyrate; MFI, mean fluorescence intensity.

Figure S8. Additional results on the role of ketogenesis in bacterial neuroinvasion, related to Figure 6.

(A-B) The KE supplemental experiment was shown in Figure 6A-6D. (A) Flow cytometry analysis of $CD36^{+}$ macrophages in mice supplemented with KE. (B) Clinical scores of mice supplemented with KE.

(C-D) The ketogenic diet experiment was shown in Figure 6E-6M. Body weight changes (C) and clinical scores (D) of mice during *L. monocytogenes* infection.

(E) Quantification of Evans blue leakage of mouse brains in Figure 6L.

(F-I) $HCAR2^{+/+}$ and $HCAR2^{-/-}$ mice were treated with ketogenic and control diets, respectively, for 4 weeks, followed by oral infection with 2×10^{8} CFU *L. monocytogenes*. (F) Survival of mice exposed to *L. monocytogenes* (n=10 for each group). (G) Bacterial burdens in organs (brain, lung, spleen, liver). Cytokine levels in plasma (H) and brain homogenate (I) (n=5 for each group).

(J-L) C57BL/6 mice were treated with ketogenic and control diets, respectively, for 4 weeks, followed by intravenous infection with 2×10^{8} CFU MRSA. (J) Survival of mice exposed to MRSA (n=15 for each group). (K) Bacterial burdens in organs (brain, lung, spleen, liver). (L) Clinical scores of mice during neuroinvasion (n=5 for each

group).

Experiments were performed in duplicate. Data are presented as mean ± SEM. *p < 0.05, **p < 0.01. Abbreviations: ns, nonsignificant; i.p., intraperitoneally.

Figure S9. Increased glucose levels alleviate bacterial neuroinvasion.

(A) Schematic diagram of *in vivo* glucose supplementation. C57BL/6 mice were challenged with 2×10^8 CFU *L. monocytogenes* and then injected intraperitoneally with glucose (100 mg/kg) every 12 hours.

(B-D) Serum glucose (B), BHB levels (C) and $CD36^+$ macrophages percentage (D) were detected every 12 hours (n=5 for each group).

(E) Survival of mice exposed to *L. monocytogenes* with or without glucose supplementation (n=10 for each group).

(F) Bacterial burdens in parenchymal organs of mice after 48 hours of infection.

(G-H) Cytokine levels in the plasma (G) and brain homogenate (H).

(I) Clinical scores of mice during L. monocytogenes infection.

Experiments were performed in duplicate. Data are presented as mean ± SEM. *p < 0.05, **p < 0.01. Abbreviations: ns, nonsignificant.

Figure S10. Additional results of high levels of BHB and human bacterial meningitis, related to Figure 7.

(A) Risk factors of bacterial meningitis from the patients in the MIMIC IV database.

(B-E) Glucose (B) and insulin (C) levels in serum from the recruited HC and BM

patients. Correlation between serum glucose level and BHB (D), as well as serum insulin levels and BHB (E) in BM patients. R, correlation coefficient

(F-H) Serum triglyceride (TC, F), high density lipoprotein (HDL-C, G) and low density lipoprotein (LDL-C, H) from HC and BM patients.

Data are presented as mean ± SEM. *$p < 0.05$, **$p < 0.01$. Abbreviations: ns, nonsignificant, HC, health control, BM, bacterial meningitis.

Materials and methods

Clinical samples

Bacterial meningitis (BM) disease subjects (n = 62, 32 males and 30 females, aged 41.62 ±15.68 years) and healthy donors (n = 60, 30 males and 30 females, aged 38.32±9.17 years) were recruited from Chongqing Public Health Medical Center. Isolation of PBMCs and single-cell suspensions was performed using PBMC Isolation Kit (P8680, Solarbio) by density gradient centrifugation. Plasma was collected from each patient and donor and then used for quantification of BHB. This study was carried out in strict accordance with the Guidelines for the Care and Use of Animals of Chongqing University, and was compliant with the “Guidance of the Ministry of Science and Technology (MOST) for the Review and Approval of Human Genetic Resources”. Healthy individuals and patients providing blood samples were given informed consent. The ethics committee approved this consent procedure. The clinical symptoms of the BM patients included burnout, headache, irritability, vomiting, fever,

1078 neck stiffness, convulsion, and consciousness disorder. Each symptom is worth 1
1079 point.
1080 The retrospective study was using Medical Information Mart for Intensive Care IV
1081 (MIMIC-IV) version 1.0 data (https://physionet.org/content/mimiciv/1.0/), which
1082 includes the medical information of ICU patients in a Boston hospital in the United
1083 States over a 10-year study period. The establishment of the database was approved
1084 by the Massachusetts Institute of Technology (Cambridge, MA) and the Institutional
1085 Review Boards of Beth Israel Deaconess Medical Center (Boston, MA). Data were
1086 extracted from the MIMIC-IV database using Structured Query Language (SQL) with
1087 Navicat Premium (version 12.0.28). A total of 128 records of admission (49 patients /
1088 79 controls) in the MIMIC IV database were included in this work. The patients with
1089 benign intracranial hypertension were regarded as the control group.
1090
1091 **Animal**
1092 All animal experiments were performed following institutional guidelines at
1093 Chongqing University. In all experiments, control and experimental mice were 6-8-
1094 week-old littermates of male C57BL/6 mice. Littermates of the same sex were housed
1095 together regardless of genotype. All mice were maintained under a 12-hour light-dark
1096 cycle with ad libitum access to regular food and water.
1097
1098 **Bacterial strains**
1099 *L. monocytogenes* (19115) and *S. pneumoniae* 49619 were grown in Brain Heart

Infusion Broth. Methicillin-resistant *Staphylococcus aureus* USA300 and *S. Typhimurium* were grown in Luria-Bertani Broth.

Data and code availability

Single-cell RNA-seq data (accession number GEO: GSE264020, secure token for reviewer: stchicgorhozbkb) and RNA-seq data (accession number GEO: GSE273820, secure token for reviewer: gbohyqeanrmzhyn) have been deposited at GEO and are publicly available as of the date of publication.

Single cell RNA-sequencing analysis

Isolated PBMCs from the mice were transported in in sterile culture dish with 10 ml Dulbecco's Phosphate-Buffered Saline (DPBS, Thermo Fisher Scientific) on ice to remove the residual tissue storage solution, then minced on ice. We used dissociation enzyme 0.25% Trypsin (Thermo Fisher Scientific) and 10 ug/mL DNase I (Sigma) dissolved in PBS with 5% Fetal Bovine Serum (FBS, GIBCO) to digest the tissues. PBMCs were dissociated at 37 ℃ under a shaking speed of 50 rpm for about 40 min. We repeatedly collected the dissociated cells at interval of 20 min to increase cell yield and viability. Cell suspensions were filtered using a 40-μm nylon cell strainer and red blood cells were removed by red blood cell lysis solution (Thermo Fisher Scientific). Dissociated cells were washed with DPBS containing 2% FBS.

10× beads were then subject to second-strand cDNA synthesis, adaptor ligation, and universal amplification. Sequencing libraries were prepared using randomly

1122 interrupted whole-transcriptome amplification products to enrich the 3' end of the
1123 transcripts linked with the cell barcode and UMI. All the remaining procedures
1124 including the library construction were performed according to the standard
1125 manufacturer's protocol (Chromium Single Cell 3' v3). Sequencing libraries were
1126 quantified using a High Sensitivity DNA Chip (Agilent) on a Bioanalyzer 2100 and
1127 the Qubit High Sensitivity DNA Assay (Thermo Fisher Scientific). The libraries were
1128 sequenced on NovaSeq6000 (Illumina) using 2×150 chemistry. The sequencing and
1129 bioinformatic analysis were performed on platform of Majorbio Co., Ltd (Shanghai,
1130 China).
1131 Reads were processed using the Cell Ranger (v7.1.0) pipeline with default and
1132 recommended parameters. FASTQs generated from Illumina sequencing output were
1133 aligned to the mouse genome, version GRCm38, using the STAR algorithm. Gene-
1134 barcode matrix containing the barcoded cells and gene expression counts were
1135 generated. This output was then imported into the Seurat (v3.2.0) R toolkit for quality
1136 control and downstream analysis of our single cell RNAseq data.
1137 Cells were clustered using graph-based clustering of the PCA reduced data with the
1138 Louvain Method after computing a shared nearest neighbor graph. For sub-clustering,
1139 we applied the same procedure of scaled, dimensionality reduction, and clustering to
1140 the specific set of data. For each cluster, we used the Wilcoxon Rank-Sum Test to find
1141 significant deferentially expressed genes comparing to the remaining clusters.
1142 To identify differential expression genes (DEGs) between two different samples or
1143 clusters, was performed using the function FindMarkers in Seurat, using a likelihood

ratio test. Essentially, DEGs with |log2FC| > 0.25 and Q value ≤0.05 were significantly different expressed genes. In addition, functional-enrichment analysis GO were performed to identify which DEGs were significantly enriched in GO terms and metabolic pathways at Bonferroni-corrected P-value ≤ 0.05 compared with the whole-transcriptome background. GO functional enrichment analysis were carried out by Goatools (https://github.com/tanghaibao/Goatools).

Mouse model of acute neuroinvasion

Mice were challenged with pathogenic bacteria (*L. monocytogenes* and MRSA, 2×10^8 CFU; *S. Typhimurium* and *S. pneumonia*, 1×10^8 CFU) to construct a model of acute bacterial meningitis. Mice challenged with LPS (2 mg/mouse) were used as positive controls for BBB damage. The progression of acute bacterial meningitis was determined by clinical scores as previously described with a few adaptations.[59] Clinical scoring was performed based on the Table S2, including activity (0–2), time to return to upright position (0–2), eyes (0–2) and neurological examination (0–2). Mice were deeply anaesthetized by an intraperitoneal injection of tribromoethanol solution (Avertin, 500 mg/kg) and transcranial perfused with saline solution for brain tissue pathomorphology. Blood was sampled immediately before perfusion. Tissue samples, including brain, lung, liver, and spleen, were dissected and weighed.

Analysis of bacterial load in cell or tissue

Tissue samples of mice were weighted and then transferred into 2 ml tubes containing

1166 4 mm stainless steel beads (Qiagen) and 1 ml of ice-cold sterile saline.
1167 Homogenization was carried out in TissueLyser II (Qiagen) for 5 min at 70 Hz. Serial
1168 dilutions of the homogenates were plated on the plates incubated at 37℃ and CFU
1169 were counted.
1170 The infected macrophages were incubated in a fresh solution containing 5 μg/mL
1171 lysostaphin for the indicated periods and then lysed by 0.2% Triton to release
1172 intracellular bacteria. The lysates were diluted to appropriate dilutions with sterile
1173 PBS for CFU count on agar plates.
1174
1175 **BBB permeability assays**
1176 After infection, mice were retro-orbitally injected with 2% Evans blue. After 2 h of
1177 circulation, mice were deeply anaesthetized, and the brains were delicately dissected
1178 after transcardial PBS perfusion. Whole-brain images were acquired using a digital
1179 camera. To quantify Evans blue leakage, mouse brains were longitudinally cut,
1180 weighted and then homogenized in 0.5 ml of 50% trichloroacetic acid. The lysates
1181 were centrifuged at 15,000 g for 30 min. The amount of extravasated Evans blue in
1182 the supernatants was measured at a Multi-Mode Microplate Reader (SpetraMax i3x)
1183 at 620/680 nm emission, calculated by a standard curve, and normalized to the weight
1184 of each brain.
1185
1186 **Brain histopathology and Immunostaining**
1187 Brain samples were collected from infected mice 24 hours after injection. Mice were

1188 deeply anaesthetized with tribromoethanol solution (Avertin, 500 mg/kg,
1189 intravenously) and transcranial perfused with 30 ml saline solution followed by 10 ml
1190 of 4% Paraformaldehyde (PFA) in saline. After dissection, brain samples were
1191 maintained in 4% PFA at 4 ℃. Fixed brains were embedded in paraffin, sectioned and
1192 half of the slides were stained using haematoxylin and eosin. Each field was assigned
1193 a score from 0 to 3 based on neuronal morphology: grade 0 (not altered); grade 1 (no
1194 vacuolation with small numbers of pyknotic cells); grade 2 (moderate vacuolation and
1195 pyknosis); and grade 3 (extensive vacuolation, pyknosis and tissue loss or liquefactive
1196 necrosis).
1197 Fresh frozen brain tissue sections of 5-10 mm thickness were mounted on slides, air
1198 dried for 10 minutes at room temperature and fixed in ice cold 10% neutral-buffered
1199 formalin for 5-10 min. Slices were washed in PBS, then incubated for 2 hours in 3%
1200 bovine serum albumin (BSA) and then 0.1% Triton X-100 in PBS. The slides were
1201 labelled with the appropriate primary antibodies of CD11b and CD36 overnight at
1202 4 ℃ in mild blocking conditions. Next day, the slices were washed in PBS, and then
1203 incubated with secondary antibodies and DAPI. Tissues were washed in PBS and then
1204 mounted on glass slides under coverslips in mounting medium. The slides were left in
1205 darkness overnight before observation under a Zeiss LSM900 or LM710 microscope.
1206
1207 **Cell sorting and flow cytometry.**
1208 Isolated mouse PBMCs were cleaned twice with PBS. After calculating and
1209 determining the appropriate concentration, appropriate amount of fluorescent-coupled

1210 primary antibody (F4/80-APC, CD11b-FITC, as the marker of macrophage, CD36-
1211 FITC) was added respectively. Incubate at 4 ℃ for 30 min away from light. The
1212 living macrophages were collected according to the expression of CD36 and then
1213 culture in vitro overnight. The sorting cells were detected the lipid content using
1214 BODIPY FL and oil Red O. To evaluate the ability of lipid uptake, macrophages were
1215 incubated with 40 μg/ml DiI-ox-LDL particles for 6h and then detect the fluorescence
1216 intensity by flow cytometry.
1217 To determine the proportion of $CD36^+$ macrophages population, cells were stained
1218 with fluorescent-coupled primary antibody (F4/80-APC, CD11b-PE, CD36-FITC) at
1219 4 ℃ for 30 min away from light. To detect the expression of LAMP1 on the cell
1220 surface, infected macrophages were cleaned twice with PBS and then stained with
1221 LAMP1-FITC at 4 ℃ for 30 min away from light. The cells were washed three times
1222 and then re-suspended in 200μl of the staining buffer for final FACS analysis. Data
1223 was analyzed with FlowJo software.
1224

1225 **Isolation and culture of primary cells**

1226 To generate peritoneal macrophages, 8-week-old mice were injected intraperitoneally
1227 with 3% thioglycolate broth. After 72 hours, peritoneal cells were harvested, and
1228 macrophages were enriched by quick adherence.
1229 Primary endothelial cells were isolated from 8 to 12-week-old male C57BL/6 mice.
1230 The cerebral cortex in the brains were separated and rolled on the filter paper to
1231 remove the meninges and choroid plexuses. A mechanical reduction was performed

by mincing the brain pieces using surgical blades. The homogenate was centrifuged (800 g, 8 min, 4℃) and the precipitate was digested in DMEM containing 1 mg/ml type II collagenase and 58.5 U/ml type I DNase for 75 min on a benchtop orbital shaker at 37 ℃. The supernatant was finally collected and centrifuged at 500 g for 8 min. The isolated cerebrovascular endothelial cells were purified by the anchoring technique. The liver and lung from an anaesthetized mouse were perfused via the portal vein sequentially with balanced salt solution containing 5 mM glucose, 0.01% sodium heparin, and 5 mM EGTA and high glucose DMEM medium containing 4 mM $CaCl_2$, 2% FBS and 0.05% collagenase IV (Sigma-Aldrich, St. Louis, MO) at a flow rate of 5 ml/min for 5 min, respectively. The following steps are similar in order to separate the liver sinusoids endothelial cells and pulmonary vascular endothelial cells.

Isolation of primary embryonic neurons and single-cell suspensions was performed using Pierce Primary Neuron Isolation Kit (88280, Thermo Scientific) by density gradient centrifugation.

In vitro blood-brain barrier

The *in vitro* BBB model was constructed with primary endothelial cells using a Transwell cell culture system. Briefly, CVECs were seeded onto the upper chamber of the Transwell pre-coated with gelatine, and cultured with the medium containing 10% FBS. The integrity of the monolayer cell was evaluated by measuring the TEER values using a Millicell-ERS voltohmmeter (Millipore). The cell monolayers with

TEER values higher than 300 Ω.cm^2 were used as the BBB model for the transmigration studies. The neurons cells were seeded onto the lower chamber of the Transwell for bacterial load.

Macrophages were exposed to *L. monocytogenes* (MOI=10) for 6 hours. After the BBB model has been constructed, the infected macrophages were digested for cell counting and added into the upper chamber. The conventional incubation time was 12 hours and then the neurons cells in the bottom chamber were lysed for penetrating bacterial quantification.

Adoptive macrophages transfer in mouse bacteria brain neuroinvasion

Peritoneal macrophages from donor mice were collected via intraperitoneal injection of thioglycolate. Following further cultivation, purified macrophages were obtained. To collect CD36$^+$ macrophages, purified macrophages were stimulated with 80 μg/ml ox-LDL over 24 hours. Recipient mice were pretreated with 3 days of CTX and then intraperitoneally given 0.2 ml normal saline or cell suspension (1×10^6 per mouse) on Day 0. After adoptive macrophages transfer, recipient mice were intraperitoneally injected with 2×10^8 CFU of *L. monocytogenes* in 12 hours and euthanized after 18 hours.

Purified peritoneal macrophages were harvested from PCSK9$^{+/+}$ and PCSK9$^{-/-}$ donor mice respectively, and then transferred to recipient mice as depicted in Figure 2J. Recipient mice were infected with 2×10^8 CFU *L. monocytogenes* 12 hours after macrophages transfer and euthanized after 24 hours.

Live-cell flow chamber assay

A flow cell system was used to test macrophages adhesion, shear resistance, crawling, and transmigration, on endothelial monolayer, which was performed as previously described.[43] Shear flow was applied by a syringe pump (PHD22/2000, Harvard Apparatus) into a microfluidic chip with a 100 μm × 1 mm× 15 mm main flowing zone. Different shear stresses were acquired by setting corresponding volumetric flow rates. Isolated macrophages were stimulated under different concentration of ox-LDL for 24 hours and then infected with *L. monocytogenes* (MOI=10) for 6 hours. Macrophages were re-suspended and stained with Hoechst. The cells were then perfused over pre-formed endothelial monolayer for 8 min at a shear stress of 0.1 dyne/cm^2. Then, the adhesion and crawling dynamics of macrophages on endothelial monolayer was recorded at 2 dyn/cm^2 for 10 min at 20× objective by a CCD camera. Images were taken from the video every second and analyzed the crawling parameters and transmigrating duration with Image J software. Here a macrophage crossing the monolayer with a 70% fluorescence intensity reduction was deemed transmigrated. For testing shear-resistant macrophage adhesion, primed macrophages were re-suspended and counted. The same number of cells (2×10^4) were completely perfused over pre-formed endothelial monolayer within 10 min. The shear stress was increased stepwise from 1 to 2, 4, 8, 16, 32 dyn/cm^2 for 30s each. Remaining adherent macrophages on endothelial monolayer were recorded at 20× objective by a CCD camera and counted using Image J software. The normalized adhesion fraction was

calculated by dividing the number of adherent macrophages at the endpoint of each shear phase by the number at the endpoint of 1 dyn/cm^2. For defining the macrophage transmigration dynamics, the time-lapse images were analyzed offline frame-by-frame every second.

Quantification of *L. monocytogenes* protrusion formation

Isolated peritoneal macrophages were stimulated under different concentration of ox-LDL for 24 hours and then infected with CFSE-labeled *L. monocytogenes* (MOI=10) for 6 hours. At 4 hours post-infection, cells were fixed, permeabilized, and labeled with mouse anti-ezrin and phalloidin-Alexa 647. Samples were analyzed using confocal microscopy. Protrusions were identified as bacteria with ezrin tails that project from host cells into neighboring. In each experiment, ten cells were scored for each condition. The lengths of ezrin comet tails were measured using ImageJ software.

Lipid metabolomics

Metabolite extraction and mass spectrometry detection was processed using Ultra-High Performance Liquid Chromatography-mass spectrometry (UHPLC-MS) of Biomarker Technologies (Beijing, China). The raw data collected using MassLynx V4.2 is processed by Progenesis QI software for peak extraction, peak alignment, and other data processing operations, based on the Progenesis QI software online METLIN database and Biomark's self-built library for identification. The theoretical

1320 fragment identification and mass deviation are within 100 ppm. After normalizing the
1321 original peak area information with the total peak area, the follow-up analysis was
1322 performed. A total of 4,625 named metabolites were retained for datasets. The R
1323 language package ropls was used to perform OPLS-DA modeling, and 200 times
1324 permutation tests was performed to verify the reliability of the model.
1325
1326 **RNA-seq (RNA Sequencing)**
1327 RNA was extracted from mouse liver tissues using a Trizol extraction and Purelink
1328 RNA kit (ThermoFisher Scientific). Bioanalyzer chips were used to assess RNA
1329 quality prior to RNA sequencing. A total amount of 1 μg RNA per sample was used as
1330 input material for the RNA sample preparations. Sequencing libraries were generated
1331 using Hieff NGS Ultima Dual-mode mRNA Library Prep Kit for lumina following
1332 manufacturer's recommendations and index codes were added to attribute sequences
1333 to each sample. The libraries were sequenced on an Illumina NovaSeq platform to
1334 generate 150 bp paired-end reads, according to the manufacturer's instructions.
1335
1336 **Measurement of ECAR**
1337 ECAR was measured using the XF Cell Mito Stress Test kit (103020-100, Seahorse
1338 Biosciences) and XF Glycolysis Stress Test kit (103020-100, Seahorse Biosciences),
1339 respectively. In brief, liver tissue were seeded into XFe24 Cell Culture Microplates
1340 and cultured in a 37 °C incubator containing 5% CO2 overnight. Three injections (10
1341 mM glucose, 1.5 μM oligomycin and 50 mM 2-DG) were performed at the indicated

1342 time. ECAR values were normalized to the total amount of proteins. ECAR
1343 parameters were calculated using Wave software (v.2.4.3, Seahorse Bioscience,
1344 Agilent Technologies) according to manufacturer instructions.
1345
1346 **Fura-4 Ca^{2+} imaging**
1347 Cells were removed from incubator and washed with PBS and then incubated with 5
1348 μM Fluo-4 AM (Beyotime) for 60 min at 37 ℃ with 0.04% Pluronic-127. After
1349 incubation, cells were washed with PBS and incubated with PBS for 30 min at 37 ℃.
1350 Fluorescence was detected with a CytoFLEX Flow Cytometer (Beckman Coulter)
1351 equipped with 488 nm excitation wavelength. As indicated, BHB (10 mM) were
1352 added into the cells pre-loaded with Fluo-4 30 s after the record. Data was analyzed
1353 with Flow Jo to determine the fluorescence intensity.
1354
1355 **Diets for *in vivo* assays**
1356 When indicated, mice were administered a supplement of 20 mg/ml ketone ester (D-
1357 β-hydroxybutyrate-(R)-1,3 butanediol monoester) in the drinking water for 4 weeks
1358 before the infection. Ketogenic diets (# XTKD01, Xietong Pharma Co.) contained
1359 10% protein and 90% fat while the control diets contained 23.2% protein, 2.8% fat
1360 and 74% sugar. Mice were consequently placed on either the ketogenic or control diet
1361 for an additional 4 weeks before infection.
1362 For the glucose supplementation experiment, mice were injected intraperitoneally
1363 with saline or glucose (100 mg/kg) every 12 hours after infection. For blood glucose

level measurement, a drop of blood was collected by snipping the very end of the tail, and the blood in the strip was analysed using the glucometer to measure the blood glucose levels.

Real-time qRT-PCR

Total RNA was isolated using an RNeasy Mini Kit (QIAGEN). The mRNA was reverse-transcribed and quantified using a HiScript II 1st Strand cDNA Synthesis Kit (Vazyme). qRT-PCR was performed on an ABI StepOnePlus PCR system (Thermo Fisher Scientific), and results were normalized to GAPDH mRNA levels. Data were analyzed using the 2-DDct method.

Statistical analysis

Statistical analysis was performed using GraphPad Prism Software. Two-group comparisons were made using two-tailed unpaired Student's t-test. One-way analysis of variance (ANOVA) with appropriate multiple comparisons tests was used to compare three independent groups. For comparisons of multiple factors, two-way ANOVA with appropriate multiple comparisons tests was used. Exact *p* values for specific group comparisons in all the figures. A value of $p < 0.05$ was considered significant. Specific details of statistical analysis are presented above or in associated figure legends.

Principal component analysis (PCA) and Spearman correlation analysis were used to judge the repeatability of the samples within group and the quantity control samples.

Differential expression was tested for normalized count data using the R package edge R, with a generalized linear model. Genes with | log2 (fold change) | ⩾ 1 and P ⩽ 0.05 were identified as differentially expressed genes. The identified compounds are searched for classification and pathway information in KEGG and HMDB databases. The difference genes of KEGG pathway enrichment significance were calculated using hypergeometric distribution test.

Reference

1. Doran, K.S., Fulde, M., Gratz, N., Kim, B.J., Nau, R., Prasadarao, N., Schubert-Unkmeir, A., Tuomanen, E.I., and Valentin-Weigand, P. (2016). Host-pathogen interactions in bacterial meningitis. Acta Neuropathol *131*, 185-209. 10.1007/s00401-015-1531-z.
2. Hasbun, R. (2022). Progress and Challenges in Bacterial Meningitis: A Review. JAMA *328*, 2147-2154. 10.1001/jama.2022.20521.
3. Langen, U.H., Ayloo, S., and Gu, C. (2019). Development and Cell Biology of the Blood-Brain Barrier. Annu Rev Cell Dev Biol *35*, 591-613. 10.1146/annurev-cellbio-100617-062608.
4. Forrester, J.V., McMenamin, P.G., and Dando, S.J. (2018). CNS infection and immune privilege. Nat Rev Neurosci *19*, 655-671. 10.1038/s41583-018-0070-8.

1408 5. Loh, L.N., Gao, G., and Tuomanen, E.I. (2017). Dissecting Bacterial Cell Wall
1409 Entry and Signaling in Eukaryotic Cells: an Actin-Dependent Pathway
1410 Parallels Platelet-Activating Factor Receptor-Mediated Endocytosis. mBio *8*.
1411 10.1128/mBio.02030-16.
1412 6. Tabusi, M., Thorsdottir, S., Lysandrou, M., Narciso, A.R., Minoia, M.,
1413 Srambickal, C.V., Widengren, J., Henriques-Normark, B., and Iovino, F.
1414 (2021). Neuronal death in pneumococcal meningitis is triggered by
1415 pneumolysin and RrgA interactions with beta-actin. PLoS Pathog *17*,
1416 e1009432. 10.1371/journal.ppat.1009432.
1417 7. Coureuil, M., Lecuyer, H., Bourdoulous, S., and Nassif, X. (2017). A journey
1418 into the brain: insight into how bacterial pathogens cross blood-brain barriers.
1419 Nat Rev Microbiol *15*, 149-159. 10.1038/nrmicro.2016.178.
1420 8. Coureuil, M., Lecuyer, H., Scott, M.G., Boularan, C., Enslen, H., Soyer, M.,
1421 Mikaty, G., Bourdoulous, S., Nassif, X., and Marullo, S. (2010).
1422 Meningococcus Hijacks a beta2-adrenoceptor/beta-Arrestin pathway to cross
1423 brain microvasculature endothelium. Cell *143*, 1149-1160.
1424 10.1016/j.cell.2010.11.035.
1425 9. Huynh, J., Donovan, J., Phu, N.H., Nghia, H.D.T., Thuong, N.T.T., and
1426 Thwaites, G.E. (2022). Tuberculous meningitis: progress and remaining
1427 questions. Lancet Neurol *21*, 450-464. 10.1016/S1474-4422(21)00435-X.
1428 10. Drevets, D.A., Dillon, M.J., Schawang, J.S., Van Rooijen, N., Ehrchen, J.,
1429 Sunderkotter, C., and Leenen, P.J. (2004). The Ly-6Chigh monocyte

subpopulation transports Listeria monocytogenes into the brain during systemic infection of mice. J Immunol *172*, 4418-4424. 10.4049/jimmunol.172.7.4418.

11. Levin, B.R., Baquero, F., Ankomah, P.P., and McCall, I.C. (2017). Phagocytes, Antibiotics, and Self-Limiting Bacterial Infections. Trends Microbiol *25*, 878-892. 10.1016/j.tim.2017.07.005.

12. Boada-Romero, E., Martinez, J., Heckmann, B.L., and Green, D.R. (2020). The clearance of dead cells by efferocytosis. Nat Rev Mol Cell Biol *21*, 398-414. 10.1038/s41580-020-0232-1.

13. Locati, M., Curtale, G., and Mantovani, A. (2020). Diversity, Mechanisms, and Significance of Macrophage Plasticity. Annu Rev Pathol *15*, 123-147. 10.1146/annurev-pathmechdis-012418-012718.

14. Zhai, L., Huang, C., Ning, Z., Zhang, Y., Zhuang, M., Yang, W., Wang, X., Wang, J., Zhang, L., Xiao, H., et al. (2023). Ruminococcus gnavus plays a pathogenic role in diarrhea-predominant irritable bowel syndrome by increasing serotonin biosynthesis. Cell Host Microbe *31*, 33-44 e35. 10.1016/j.chom.2022.11.006.

15. Van der Merwe, S., Chokshi, S., Bernsmeier, C., and Albillos, A. (2021). The multifactorial mechanisms of bacterial infection in decompensated cirrhosis. J Hepatol *75 Suppl 1*, S82-S100. 10.1016/j.jhep.2020.11.029.

16. Maudet, C., Kheloufi, M., Levallois, S., Gaillard, J., Huang, L., Gaultier, C., Tsai, Y.H., Disson, O., and Lecuit, M. (2022). Bacterial inhibition of Fas-

mediated killing promotes neuroinvasion and persistence. Nature *603*, 900-906. 10.1038/s41586-022-04505-7.

17. Xu, K., Yin, N., Peng, M., Stamatiades, E.G., Shyu, A., Li, P., Zhang, X., Do, M.H., Wang, Z., Capistrano, K.J., et al. (2021). Glycolysis fuels phosphoinositide 3-kinase signaling to bolster T cell immunity. Science *371*, 405-410. 10.1126/science.abb2683.

18. Escoll, P., Song, O.R., Viana, F., Steiner, B., Lagache, T., Olivo-Marin, J.C., Impens, F., Brodin, P., Hilbi, H., and Buchrieser, C. (2017). Legionella pneumophila Modulates Mitochondrial Dynamics to Trigger Metabolic Repurposing of Infected Macrophages. Cell Host Microbe *22*, 302-316 e307. 10.1016/j.chom.2017.07.020.

19. Yang, D., Jacobson, A., Meerschaert, K.A., Sifakis, J.J., Wu, M., Chen, X., Yang, T., Zhou, Y., Anekal, P.V., Rucker, R.A., et al. (2022). Nociceptor neurons direct goblet cells via a CGRP-RAMP1 axis to drive mucus production and gut barrier protection. Cell *185*, 4190-4205 e4125. 10.1016/j.cell.2022.09.024.

20. Loft, A., Schmidt, S.F., Caratti, G., Stifel, U., Havelund, J., Sekar, R., Kwon, Y., Sulaj, A., Chow, K.K., Alfaro, A.J., et al. (2022). A macrophage-hepatocyte glucocorticoid receptor axis coordinates fasting ketogenesis. Cell Metab *34*, 473-486 e479. 10.1016/j.cmet.2022.01.004.

21. Lu, J.F., Zhu, M.Q., Xia, B., Zhang, N.N., Liu, X.P., Liu, H., Zhang, R.X., Xiao, J.Y., Yang, H., Zhang, Y.Q., et al. (2023). GDF15 is a major determinant

of ketogenic diet-induced weight loss. Cell Metab *35*, 2165-2182 e2167. 10.1016/j.cmet.2023.11.003.

22. Tomlinson, K.L., Chen, Y.T., Junker, A., Urso, A., Wong Fok Lung, T., Ahn, D., Hofstaedter, C.E., Baskota, S.U., Ernst, R.K., Prince, A., and Riquelme, S.A. (2023). Ketogenesis promotes tolerance to Pseudomonas aeruginosa pulmonary infection. Cell Metab *35*, 1767-1781 e1766. 10.1016/j.cmet.2023.09.001.

23. Goldberg, E.L., Molony, R.D., Kudo, E., Sidorov, S., Kong, Y., Dixit, V.D., and Iwasaki, A. (2019). Ketogenic diet activates protective gammadelta T cell responses against influenza virus infection. Sci Immunol *4*. 10.1126/sciimmunol.aav2026.

24. Karagiannis, F., Peukert, K., Surace, L., Michla, M., Nikolka, F., Fox, M., Weiss, P., Feuerborn, C., Maier, P., Schulz, S., et al. (2022). Impaired ketogenesis ties metabolism to T cell dysfunction in COVID-19. Nature *609*, 801-807. 10.1038/s41586-022-05128-8.

25. Seufert, A.L., Hickman, J.W., Traxler, S.K., Peterson, R.M., Waugh, T.A., Lashley, S.J., Shulzhenko, N., Napier, R.J., and Napier, B.A. (2022). Enriched dietary saturated fatty acids induce trained immunity via ceramide production that enhances severity of endotoxemia and clearance of infection. Elife *11*. 10.7554/eLife.76744.

26. Wilhelm, C., Surendar, J., and Karagiannis, F. (2021). Enemy or ally? Fasting as an essential regulator of immune responses. Trends Immunol *42*, 389-400.

10.1016/j.it.2021.03.007.

27. Singh, V., Jamwal, S., Jain, R., Verma, P., Gokhale, R., and Rao, K.V. (2012). Mycobacterium tuberculosis-driven targeted recalibration of macrophage lipid homeostasis promotes the foamy phenotype. Cell Host Microbe *12*, 669-681. 10.1016/j.chom.2012.09.012.

28. McFarland, A.P., Yalin, A., Wang, S.Y., Cortez, V.S., Landsberger, T., Sudan, R., Peng, V., Miller, H.L., Ricci, B., David, E., et al. (2021). Multi-tissue single-cell analysis deconstructs the complex programs of mouse natural killer and type 1 innate lymphoid cells in tissues and circulation. Immunity *54*, 1320-1337 e1324. 10.1016/j.immuni.2021.03.024.

29. Ahmad, F., Rani, A., Alam, A., Zarin, S., Pandey, S., Singh, H., Hasnain, S.E., and Ehtesham, N.Z. (2022). Macrophage: A Cell With Many Faces and Functions in Tuberculosis. Front Immunol *13*, 747799. 10.3389/fimmu.2022.747799.

30. Hill, D.A., Lim, H.W., Kim, Y.H., Ho, W.Y., Foong, Y.H., Nelson, V.L., Nguyen, H.C.B., Chegireddy, K., Kim, J., Habertheuer, A., et al. (2018). Distinct macrophage populations direct inflammatory versus physiological changes in adipose tissue. Proc Natl Acad Sci U S A *115*, E5096-E5105. 10.1073/pnas.1802611115.

31. Jaitin, D.A., Adlung, L., Thaiss, C.A., Weiner, A., Li, B., Descamps, H., Lundgren, P., Bleriot, C., Liu, Z., Deczkowska, A., et al. (2019). Lipid-Associated Macrophages Control Metabolic Homeostasis in a Trem2-

1518 Dependent Manner. Cell *178*, 686-698 e614. 10.1016/j.cell.2019.05.054.

1519 32. Luis, G., Godfroid, A., Nishiumi, S., Cimino, J., Blacher, S., Maquoi, E.,
1520 Wery, C., Collignon, A., Longuespee, R., Montero-Ruiz, L., et al. (2021).
1521 Tumor resistance to ferroptosis driven by Stearoyl-CoA Desaturase-1 (SCD1)
1522 in cancer cells and Fatty Acid Biding Protein-4 (FABP4) in tumor
1523 microenvironment promote tumor recurrence. Redox Biol *43*, 102006.
1524 10.1016/j.redox.2021.102006.

1525 33. Victor, M.B., Leary, N., Luna, X., Meharena, H.S., Scannail, A.N., Bozzelli,
1526 P.L., Samaan, G., Murdock, M.H., von Maydell, D., Effenberger, A.H., et al.
1527 (2022). Lipid accumulation induced by APOE4 impairs microglial
1528 surveillance of neuronal-network activity. Cell Stem Cell *29*, 1197-1212
1529 e1198. 10.1016/j.stem.2022.07.005.

1530 34. Chen, Y., Zhang, J., Cui, W., and Silverstein, R.L. (2022). CD36, a signaling
1531 receptor and fatty acid transporter that regulates immune cell metabolism and
1532 fate. J Exp Med *219*. 10.1084/jem.20211314.

1533 35. Botham, K.M., and Wheeler-Jones, C.P. (2013). Postprandial lipoproteins and
1534 the molecular regulation of vascular homeostasis. Prog Lipid Res *52*, 446-464.
1535 10.1016/j.plipres.2013.06.001.

1536 36. Jaggi, U., Matundan, H.H., Yu, J., Hirose, S., Mueller, M., Wormley, F.L., Jr.,
1537 and Ghiasi, H. (2021). Essential role of M1 macrophages in blocking cytokine
1538 storm and pathology associated with murine HSV-1 infection. PLoS Pathog
1539 *17*, e1009999. 10.1371/journal.ppat.1009999.

37. Pasula, R., Martin, W.J., 2nd, Kesavalu, B.R., Abdalla, M.Y., and Britigan, B.E. (2017). Passive transfer of interferon-gamma over-expressing macrophages enhances resistance of SCID mice to Mycobacterium tuberculosis infection. Cytokine *95*, 70-79. 10.1016/j.cyto.2017.02.009.

38. Peyrusson, F., Varet, H., Nguyen, T.K., Legendre, R., Sismeiro, O., Coppee, J.Y., Wolz, C., Tenson, T., and Van Bambeke, F. (2020). Intracellular Staphylococcus aureus persisters upon antibiotic exposure. Nat Commun *11*, 2200. 10.1038/s41467-020-15966-7.

39. Ding, Z., Pothineni, N.V.K., Goel, A., Luscher, T.F., and Mehta, J.L. (2020). PCSK9 and inflammation: role of shear stress, pro-inflammatory cytokines, and LOX-1. Cardiovasc Res *116*, 908-915. 10.1093/cvr/cvz313.

40. Da Dalt, L., Castiglioni, L., Baragetti, A., Audano, M., Svecla, M., Bonacina, F., Pedretti, S., Uboldi, P., Benzoni, P., Giannetti, F., et al. (2021). PCSK9 deficiency rewires heart metabolism and drives heart failure with preserved ejection fraction. Eur Heart J *42*, 3078-3090. 10.1093/eurheartj/ehab431.

41. Katsuki, S., P, K.J., Lupieri, A., Nakano, T., Passos, L.S.A., Rogers, M.A., Becker-Greene, D., Le, T.D., Decano, J.L., Ho Lee, L., et al. (2022). Proprotein Convertase Subtilisin/Kexin 9 (PCSK9) Promotes Macrophage Activation via LDL Receptor-Independent Mechanisms. Circ Res *131*, 873-889. 10.1161/CIRCRESAHA.121.320056.

42. Qi, Z., Hu, L., Zhang, J., Yang, W., Liu, X., Jia, D., Yao, Z., Chang, L., Pan, G., Zhong, H., et al. (2021). PCSK9 (Proprotein Convertase Subtilisin/Kexin

9) Enhances Platelet Activation, Thrombosis, and Myocardial Infarct Expansion by Binding to Platelet CD36. Circulation *143*, 45-61. 10.1161/CIRCULATIONAHA.120.046290.

43. Yang, H., Li, N., Du, Y., Tong, C., Lu, S., Hu, J., Zhang, Y., and Long, M. (2017). Neutrophil adhesion and crawling dynamics on liver sinusoidal endothelial cells under shear flow. Exp Cell Res *351*, 91-99. 10.1016/j.yexcr.2017.01.002.

44. Neupane, A.S., Willson, M., Chojnacki, A.K., Vargas, E.S.C.F., Morehouse, C., Carestia, A., Keller, A.E., Peiseler, M., DiGiandomenico, A., Kelly, M.M., et al. (2020). Patrolling Alveolar Macrophages Conceal Bacteria from the Immune System to Maintain Homeostasis. Cell *183*, 110-125 e111. 10.1016/j.cell.2020.08.020.

45. Hernandez, G.E., and Iruela-Arispe, M.L. (2020). The many flavors of monocyte/macrophage--endothelial cell interactions. Curr Opin Hematol *27*, 181-189. 10.1097/MOH.0000000000000573.

46. Pang, X., He, X., Qiu, Z., Zhang, H., Xie, R., Liu, Z., Gu, Y., Zhao, N., Xiang, Q., and Cui, Y. (2023). Targeting integrin pathways: mechanisms and advances in therapy. Signal Transduct Target Ther *8*, 1. 10.1038/s41392-022-01259-6.

47. Deng, L., Kersten, S., and Stienstra, R. (2023). Triacylglycerol uptake and handling by macrophages: From fatty acids to lipoproteins. Prog Lipid Res *92*, 101250. 10.1016/j.plipres.2023.101250.

48. Patterson, M.T., Firulyova, M.M., Xu, Y., Hillman, H., Bishop, C., Zhu, A.,

Hickok, G.H., Schrank, P.R., Ronayne, C.E., Caillot, Z., et al. (2023). Trem2 promotes foamy macrophage lipid uptake and survival in atherosclerosis. Nature Cardiovascular Research *2*, 1015-1031. 10.1038/s44161-023-00354-3.

49. Andrews, N.W., and Corrotte, M. (2018). Plasma membrane repair. Curr Biol *28*, R392-R397. 10.1016/j.cub.2017.12.034.

50. Jimenez, A.J., Maiuri, P., Lafaurie-Janvore, J., Divoux, S., Piel, M., and Perez, F. (2014). ESCRT machinery is required for plasma membrane repair. Science *343*, 1247136. 10.1126/science.1247136.

51. Newman, J.C., and Verdin, E. (2017). beta-Hydroxybutyrate: A Signaling Metabolite. Annu Rev Nutr *37*, 51-76. 10.1146/annurev-nutr-071816-064916.

52. Youm, Y.H., Nguyen, K.Y., Grant, R.W., Goldberg, E.L., Bodogai, M., Kim, D., D'Agostino, D., Planavsky, N., Lupfer, C., Kanneganti, T.D., et al. (2015). The ketone metabolite beta-hydroxybutyrate blocks NLRP3 inflammasome-mediated inflammatory disease. Nat Med *21*, 263-269. 10.1038/nm.3804.

53. Duking, T., Spieth, L., Berghoff, S.A., Piepkorn, L., Schmidke, A.M., Mitkovski, M., Kannaiyan, N., Hosang, L., Scholz, P., Shaib, A.H., et al. (2022). Ketogenic diet uncovers differential metabolic plasticity of brain cells. Sci Adv *8*, eabo7639. 10.1126/sciadv.abo7639.

54. Matsuura, T.R., Puchalska, P., Crawford, P.A., and Kelly, D.P. (2023). Ketones and the Heart: Metabolic Principles and Therapeutic Implications. Circ Res *132*, 882-898. 10.1161/CIRCRESAHA.123.321872.

55. Shah, U.A., and Iyengar, N.M. (2022). Plant-Based and Ketogenic Diets As

Diverging Paths to Address Cancer: A Review. JAMA Oncol *8*, 1201-1208. 10.1001/jamaoncol.2022.1769.

56. Steeb, B., Claudi, B., Burton, N.A., Tienz, P., Schmidt, A., Farhan, H., Maze, A., and Bumann, D. (2013). Parallel exploitation of diverse host nutrients enhances Salmonella virulence. PLoS Pathog *9*, e1003301. 10.1371/journal.ppat.1003301.

57. Peyron, P., Vaubourgeix, J., Poquet, Y., Levillain, F., Botanch, C., Bardou, F., Daffe, M., Emile, J.F., Marchou, B., Cardona, P.J., et al. (2008). Foamy macrophages from tuberculous patients' granulomas constitute a nutrient-rich reservoir for M. tuberculosis persistence. PLoS Pathog *4*, e1000204. 10.1371/journal.ppat.1000204.

58. Yang, Y., Fang, H., Xie, Z., Ren, F., Yan, L., Zhang, M., Xu, G., Song, Z., Chen, Z., Sun, W., et al. (2024). Yersinia infection induces glucose depletion and AMPK-dependent inhibition of pyroptosis in mice. Nat Microbiol. 10.1038/s41564-024-01734-6.

59. Koopmans, M.M., Engelen-Lee, J., Brouwer, M.C., Jaspers, V., Man, W.K., Vall Seron, M., and van de Beek, D. (2018). Characterization of a Listeria monocytogenes meningitis mouse model. J Neuroinflammation *15*, 257. 10.1186/s12974-018-1293-3.

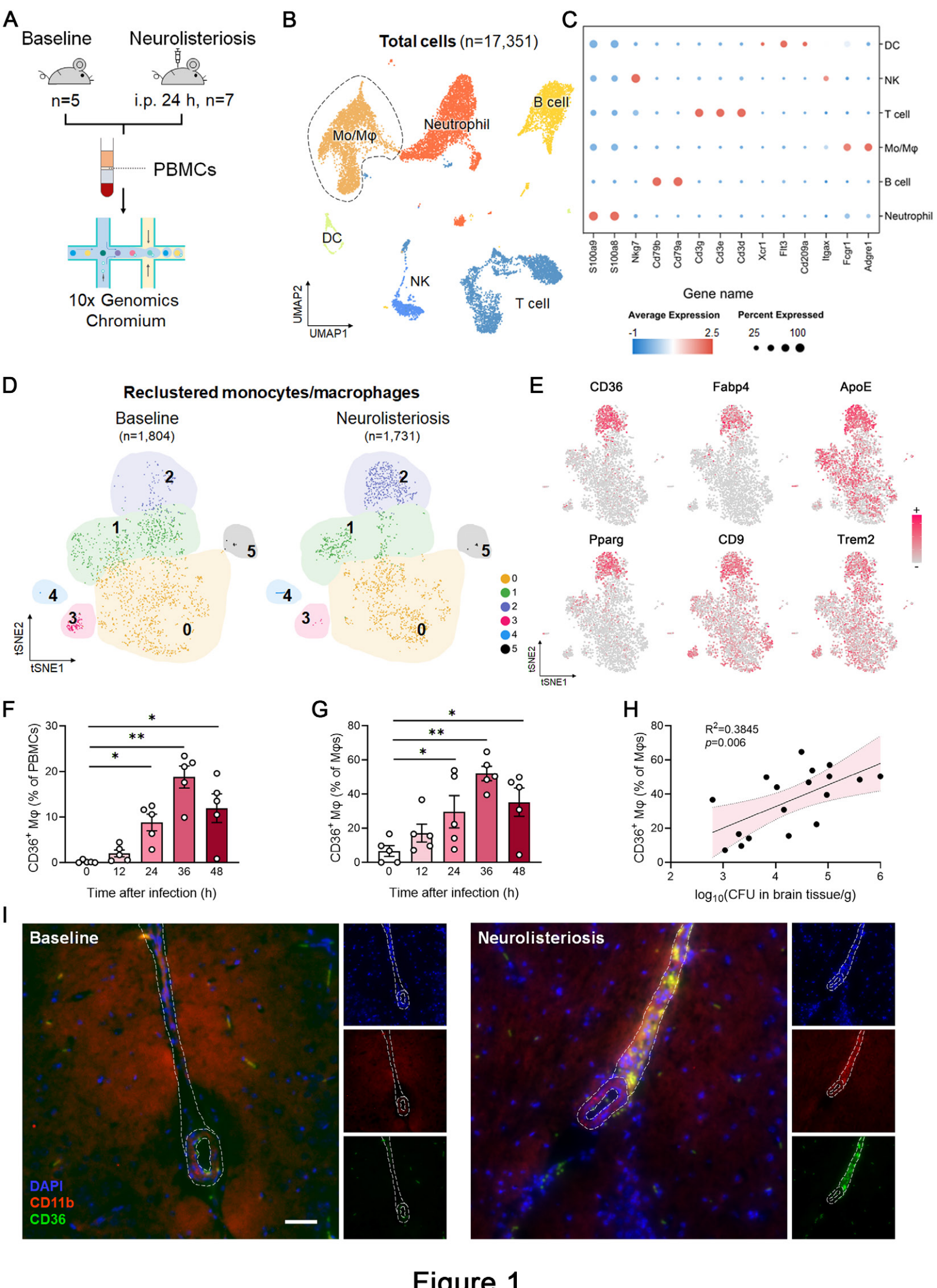
A
Baseline
Neurolisteriosis
n=5
i.p. 24 h, n=7
PBMCs
10x Genomics
Chromium
B
Total cells (n=17,351)
Mo/Mφ
Neutrophil
B cell
DC
NK
T cell
UMAP2
UMAP1
C
DC
NK
T cell
Mo/Mφ
B cell
Neutrophil
S100a9
S100a8
Nkg7
Cd79b
Cd79a
Cd3g
Cd3e
Cd3d
Xcr1
Flt3
Cd209a
Itgax
Fcgr1
Adgre1
Gene name
Average Expression
-1
2.5
Percent Expressed
25
100
D
Reclustered monocytes/macrophages
Baseline
(n=1,804)
Neurolisteriosis
(n=1,731)
tSNE2
tSNE1
E
CD36
Fabp4
ApoE
Pparg
CD9
Trem2
F
CD36+ Mφ (% of PBMCs)
Time after infection (h)
G
CD36+ Mφ (% of Mφs)
Time after infection (h)
H
R2=0.3845
p=0.006
CD36+ Mφ (% of Mφs)
log10(CFU in brain tissue/g)
I
Baseline
Neurolisteriosis
DAPI
CD11b
CD36

Figure 1

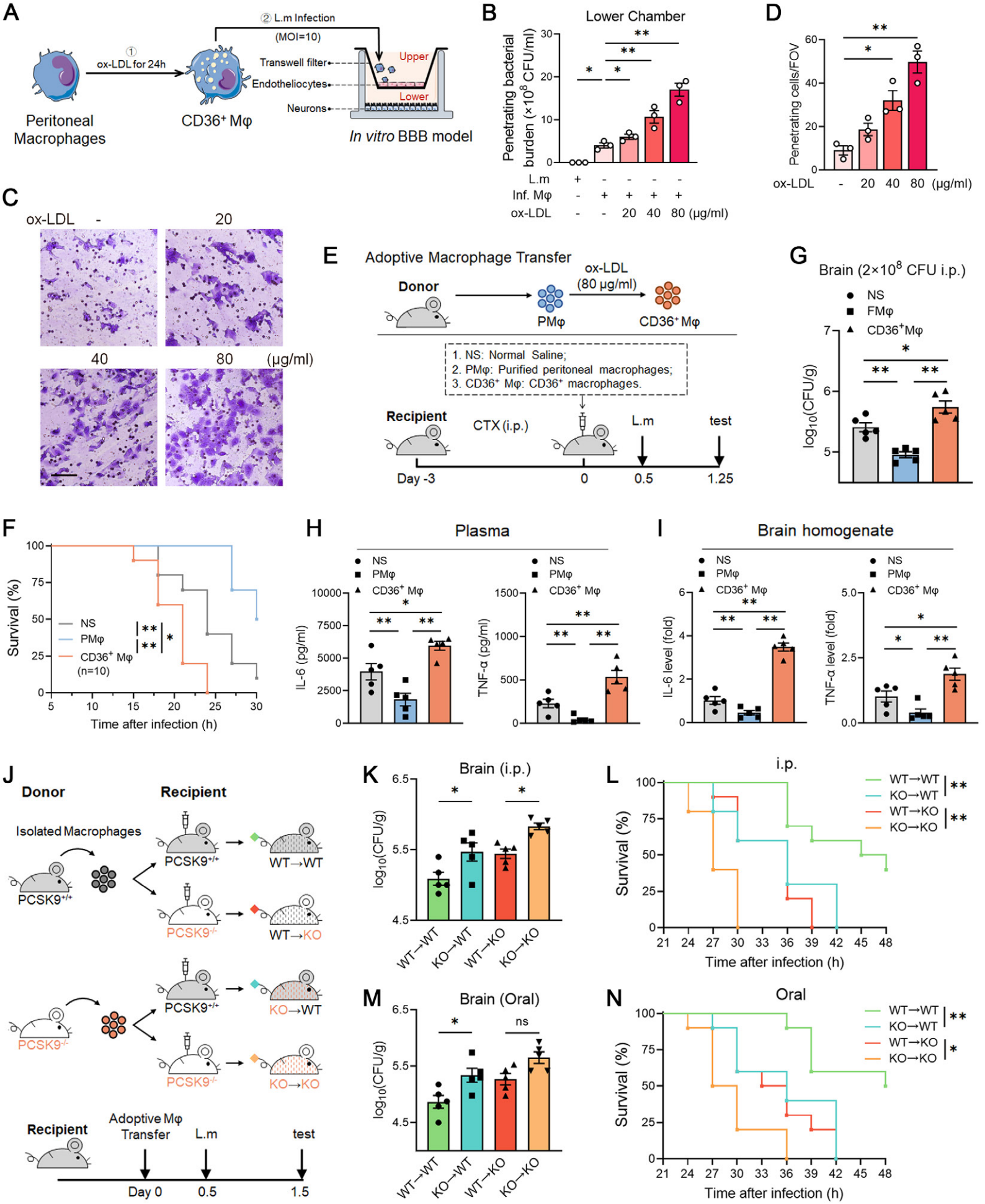
A
① ox-LDL for 24h
② L.m Infection (MOI=10)
Peritoneal Macrophages
CD36⁺ Mφ
Transwell filter
Endotheliocytes
Neurons
Upper
Lower
In vitro BBB model
B
Lower Chamber
Penetrating bacterial burden (×10⁸ CFU/ml)
L.m
Inf. Mφ
ox-LDL
D
Penetrating cells/FOV
ox-LDL - 20 40 80 (μg/ml)
C
ox-LDL - 20 40 80 (μg/ml)
E
Adoptive Macrophage Transfer
Donor
ox-LDL (80 μg/ml)
PMφ
CD36⁺ Mφ
1. NS: Normal Saline;
2. PMφ: Purified peritoneal macrophages;
3. CD36⁺ Mφ: CD36⁺ macrophages.
Recipient
CTX (i.p.)
L.m
test
Day -3
0
0.5
1.25
G
Brain (2×10⁸ CFU i.p.)
NS
FMφ
CD36⁺Mφ
log10(CFU/g)
F
Survival (%)
NS
PMφ
CD36⁺ Mφ (n=10)
Time after infection (h)
H
Plasma
IL-6 (pg/ml)
TNF-α (pg/ml)
I
Brain homogenate
IL-6 level (fold)
TNF-α level (fold)
J
Donor
Recipient
Isolated Macrophages
PCSK9⁺/⁺
PCSK9⁻/⁻
WT→WT
WT→KO
KO→WT
KO→KO
Recipient
Adoptive Mφ Transfer
L.m
test
Day 0
0.5
1.5
K
Brain (i.p.)
log10(CFU/g)
WT→WT
KO→WT
WT→KO
KO→KO
L
i.p.
Survival (%)
Time after infection (h)
M
Brain (Oral)
ns
N
Oral

Figure 2

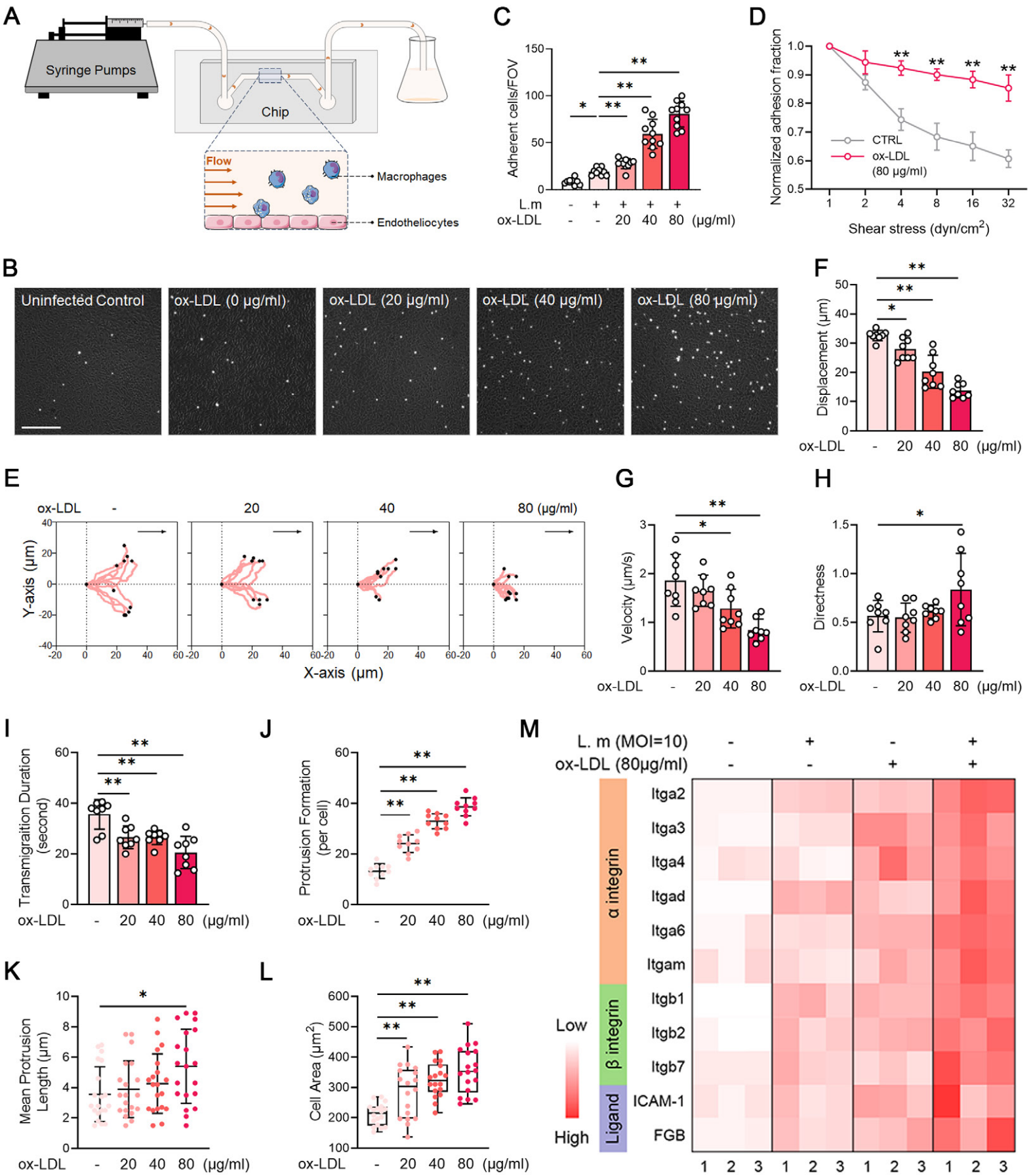
A
Syringe Pumps
Chip
Flow
Macrophages
Endotheliocytes
C
Adherent cells/FOV
L.m
ox-LDL
(μg/ml)
D
Normalized adhesion fraction
CTRL
ox-LDL
(80 μg/ml)
Shear stress (dyn/cm2)
B
Uninfected Control
ox-LDL (0 μg/ml)
ox-LDL (20 μg/ml)
ox-LDL (40 μg/ml)
ox-LDL (80 μg/ml)
F
Displacement (μm)
ox-LDL
E
Y-axis (μm)
X-axis (μm)
G
Velocity (μm/s)
H
Directness
I
Transmigraition Duration (second)
J
Protrusion Formation (per cell)
K
Mean Protrusion Length (μm)
L
Cell Area (μm2)
M
L. m (MOI=10)
ox-LDL (80μg/ml)
α integrin
β integrin
Ligand
Itga2
Itga3
Itga4
Itgad
Itga6
Itgam
Itgb1
Itgb2
Itgb7
ICAM-1
FGB
Low
High

Figure 3

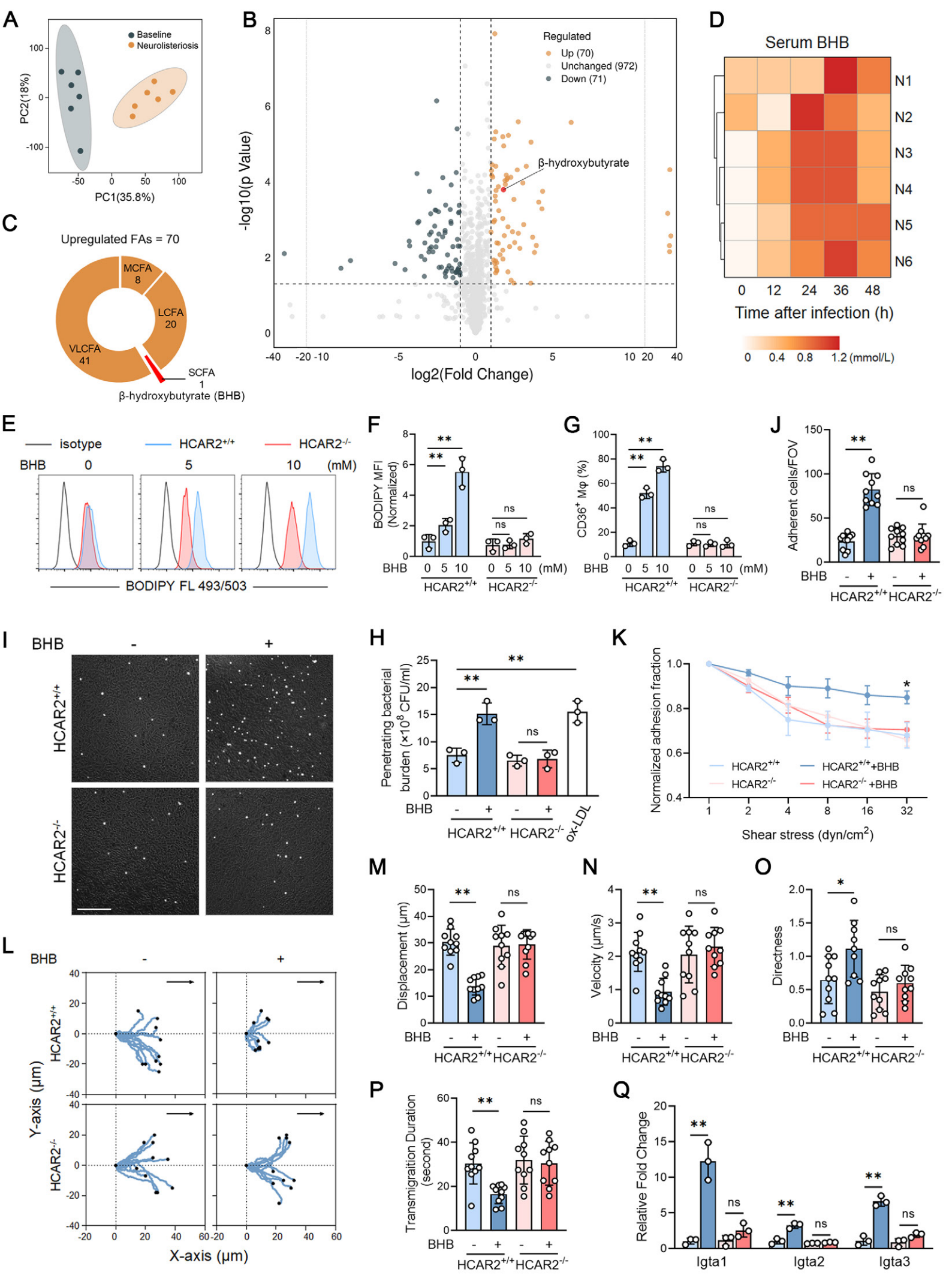
A
Baseline
Neurolisteriosis
PC2(18%)
PC1(35.8%)
B
Regulated
Up (70)
Unchanged (972)
Down (71)
β-hydroxybutyrate
-log10(p Value)
log2(Fold Change)
C
Upregulated FAs = 70
MCFA 8
LCFA 20
VLCFA 41
SCFA 1
β-hydroxybutyrate (BHB)
D
Serum BHB
N1
N2
N3
N4
N5
N6
Time after infection (h)
(mmol/L)
E
isotype
HCAR2+/+
HCAR2-/-
BHB
(mM)
BODIPY FL 493/503
F
BODIPY MFI (Normalized)
G
CD36+ Mφ (%)
J
Adherent cells/FOV
I
BHB
HCAR2+/+
HCAR2-/-
H
Penetrating bacterial burden (×10^8 CFU/ml)
ox-LDL
K
Normalized adhesion fraction
HCAR2+/+
HCAR2-/-
HCAR2+/+ +BHB
HCAR2-/- +BHB
Shear stress (dyn/cm2)
L
Y-axis (μm)
X-axis (μm)
M
Displacement (μm)
N
Velocity (μm/s)
O
Directness
P
Transmigraition Duration (second)
Q
Relative Fold Change
Igta1
Igta2
Igta3

Figure 4

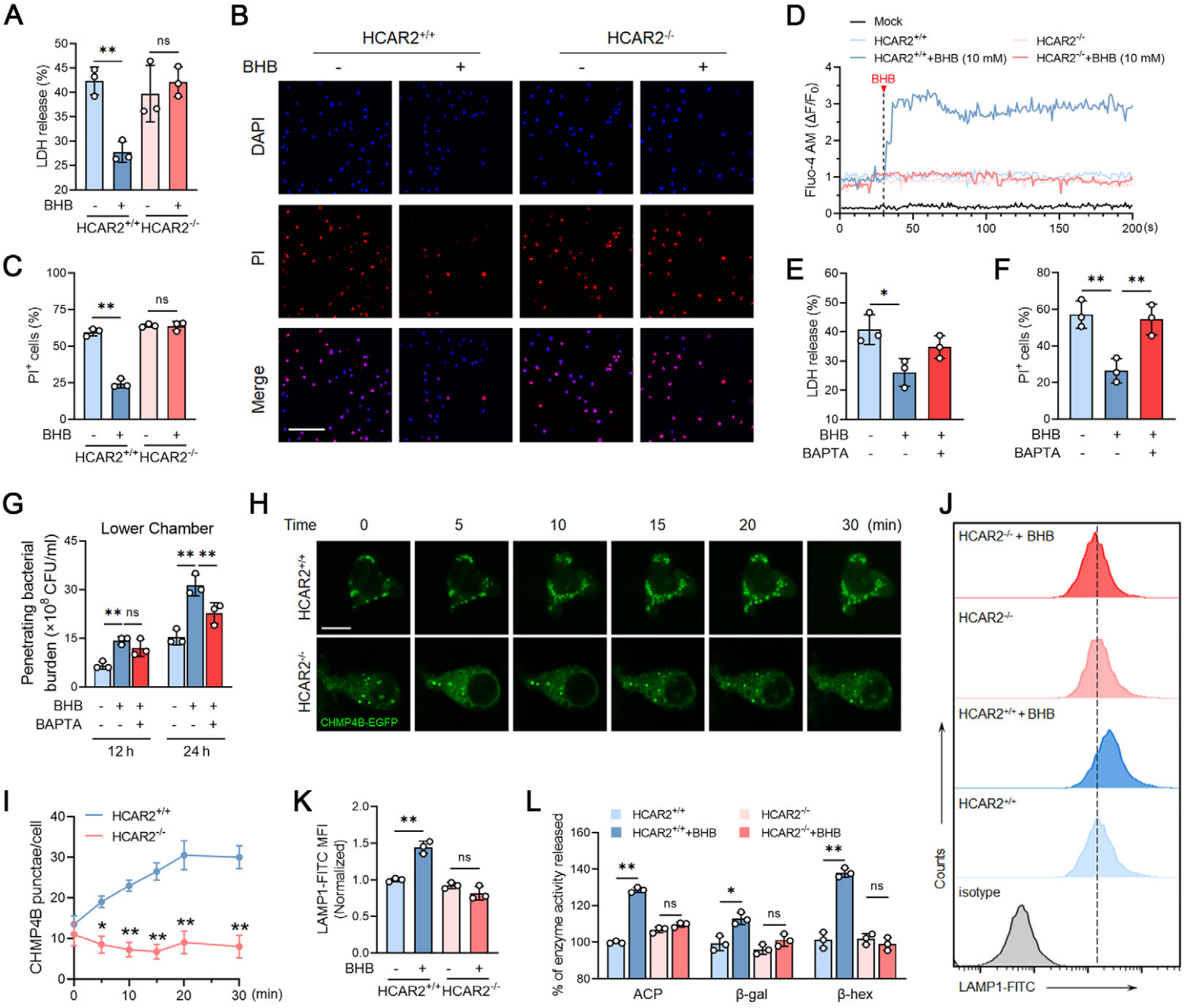
A
LDH release (%)
BHB
HCAR2+/+ HCAR2-/-
B
HCAR2+/+
HCAR2-/-
BHB
DAPI
PI
Merge
C
PI+ cells (%)
D
Mock
HCAR2+/+
HCAR2-/-
HCAR2+/+ +BHB (10 mM)
HCAR2-/- +BHB (10 mM)
BHB
Fluo-4 AM (ΔF/F0)
E
LDH release (%)
BAPTA
F
PI+ cells (%)
G
Lower Chamber
Penetrating bacterial burden (×10^8 CFU/ml)
12 h
24 h
H
Time
0
5
10
15
20
30 (min)
CHMP4B-EGFP
I
CHMP4B punctae/cell
(min)
J
HCAR2-/- + BHB
HCAR2-/-
HCAR2+/+ + BHB
HCAR2+/+
isotype
Counts
LAMP1-FITC
K
LAMP1-FITC MFI (Normalized)
L
% of enzyme activity released
HCAR2+/+ +BHB
HCAR2-/- +BHB
ACP
β-gal
β-hex

Figure 5

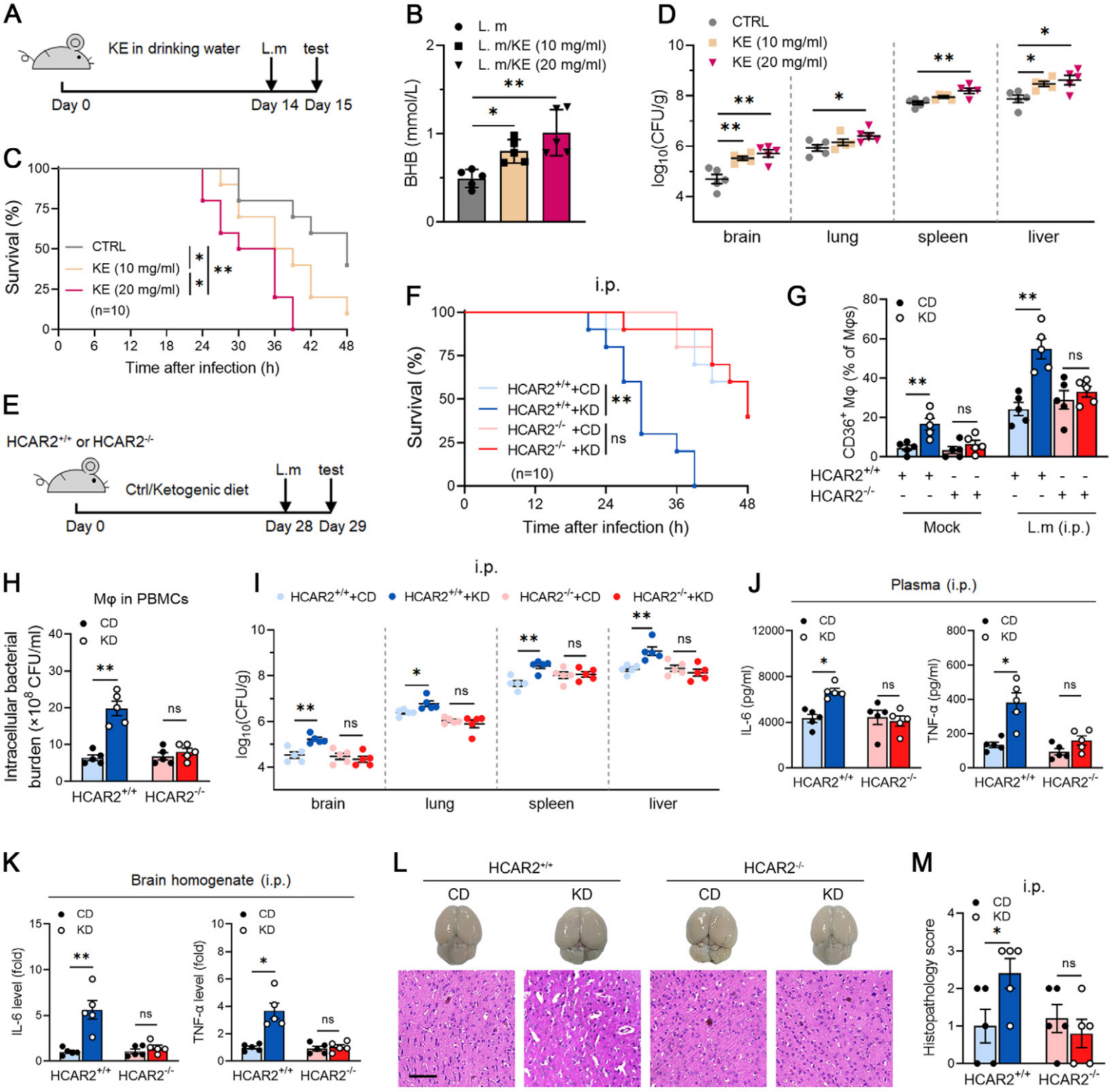
A
KE in drinking water
L.m
test
Day 0
Day 14
Day 15
B
L. m
L. m/KE (10 mg/ml)
L. m/KE (20 mg/ml)
BHB (mmol/L)
C
Survival (%)
CTRL
KE (10 mg/ml)
KE (20 mg/ml)
(n=10)
Time after infection (h)
D
CTRL
KE (10 mg/ml)
KE (20 mg/ml)
log10(CFU/g)
brain
lung
spleen
liver
E
HCAR2+/+ or HCAR2-/-
Ctrl/Ketogenic diet
L.m
test
Day 0
Day 28
Day 29
F
i.p.
Survival (%)
HCAR2+/++CD
HCAR2+/++KD
HCAR2-/- +CD
HCAR2-/- +KD
(n=10)
Time after infection (h)
G
CD
KD
CD36+ Mφ (% of Mφs)
HCAR2+/+
HCAR2-/-
Mock
L.m (i.p.)
H
Mφ in PBMCs
CD
KD
Intracellular bacterial burden (×10^8 CFU/ml)
HCAR2+/+
HCAR2-/-
I
i.p.
HCAR2+/++CD
HCAR2+/++KD
HCAR2-/-+CD
HCAR2-/-+KD
log10(CFU/g)
brain
lung
spleen
liver
J
Plasma (i.p.)
CD
KD
IL-6 (pg/ml)
TNF-α (pg/ml)
HCAR2+/+
HCAR2-/-
K
Brain homogenate (i.p.)
CD
KD
IL-6 level (fold)
TNF-α level (fold)
HCAR2+/+
HCAR2-/-
L
HCAR2+/+
HCAR2-/-
CD
KD
M
i.p.
CD
KD
Histopathology score
HCAR2+/+
HCAR2-/-

Figure 6

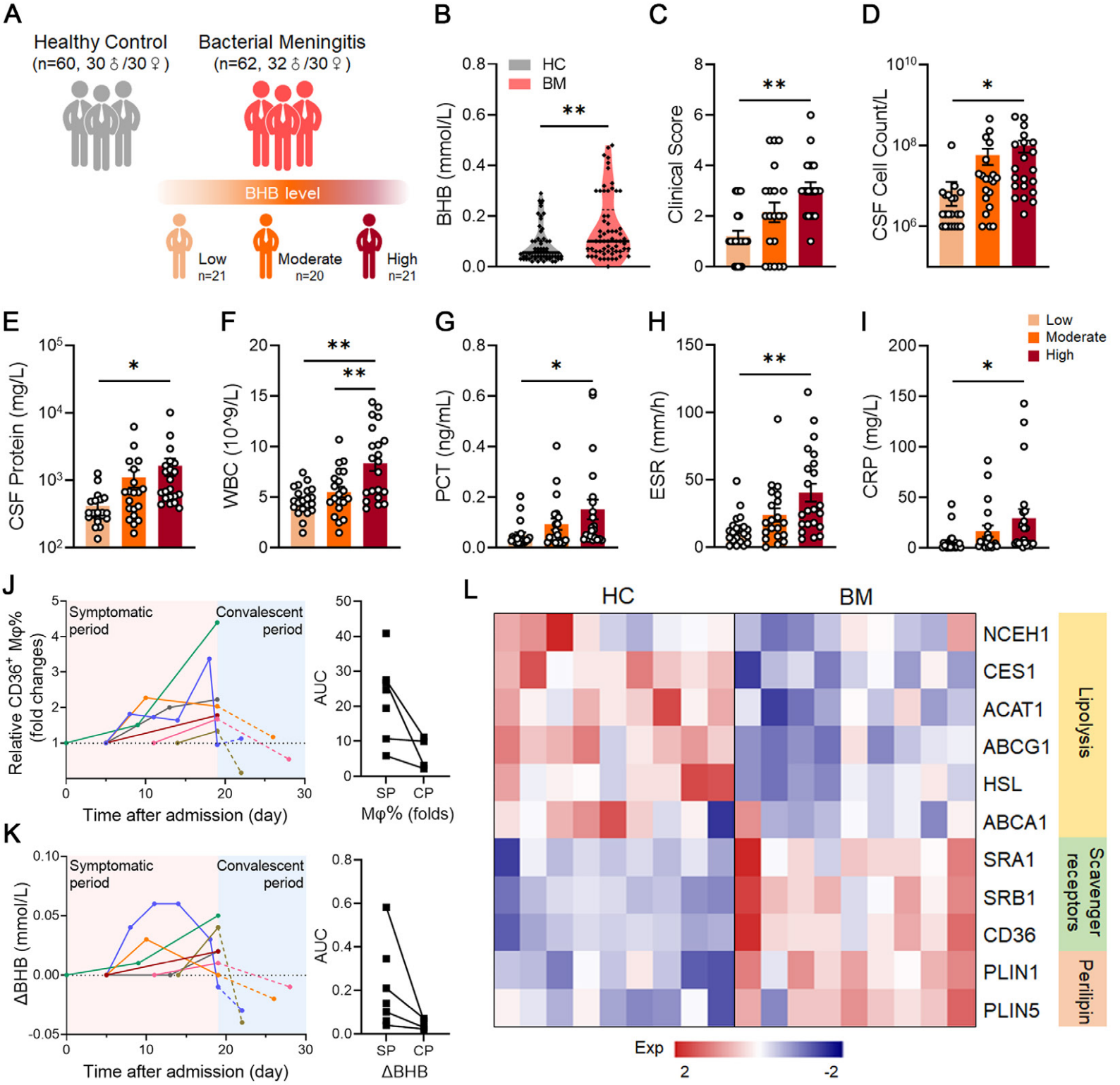
A
Healthy Control
(n=60, 30♂/30♀)
Bacterial Meningitis
(n=62, 32♂/30♀)
BHB level
Low
n=21
Moderate
n=20
High
n=21
B
HC
BM
BHB (mmol/L)
C
Clinical Score
D
CSF Cell Count/L
E
CSF Protein (mg/L)
F
WBC (10^9/L)
G
PCT (ng/mL)
H
ESR (mm/h)
I
CRP (mg/L)
Low
Moderate
High
J
Relative CD36+ Mφ%
(fold changes)
Symptomatic
period
Convalescent
period
Time after admission (day)
AUC
SP
CP
Mφ% (folds)
K
ΔBHB (mmol/L)
ΔBHB
L
HC
BM
NCEH1
CES1
ACAT1
ABCG1
HSL
ABCA1
SRA1
SRB1
CD36
PLIN1
PLIN5
Lipolysis
Scavenger receptors
Perilipin
Exp
2
-2

Figure 7

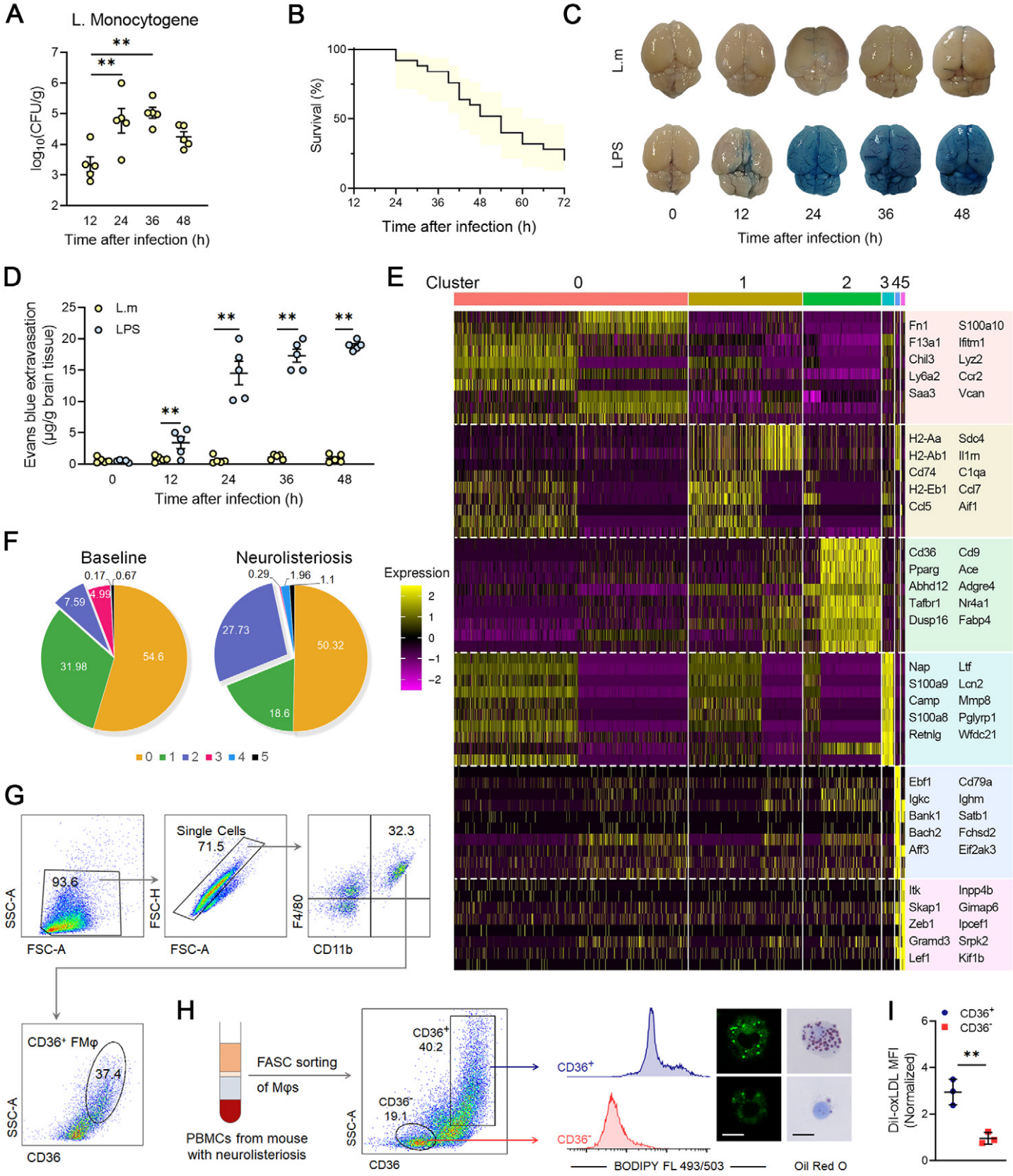

Supplementary Figure 1

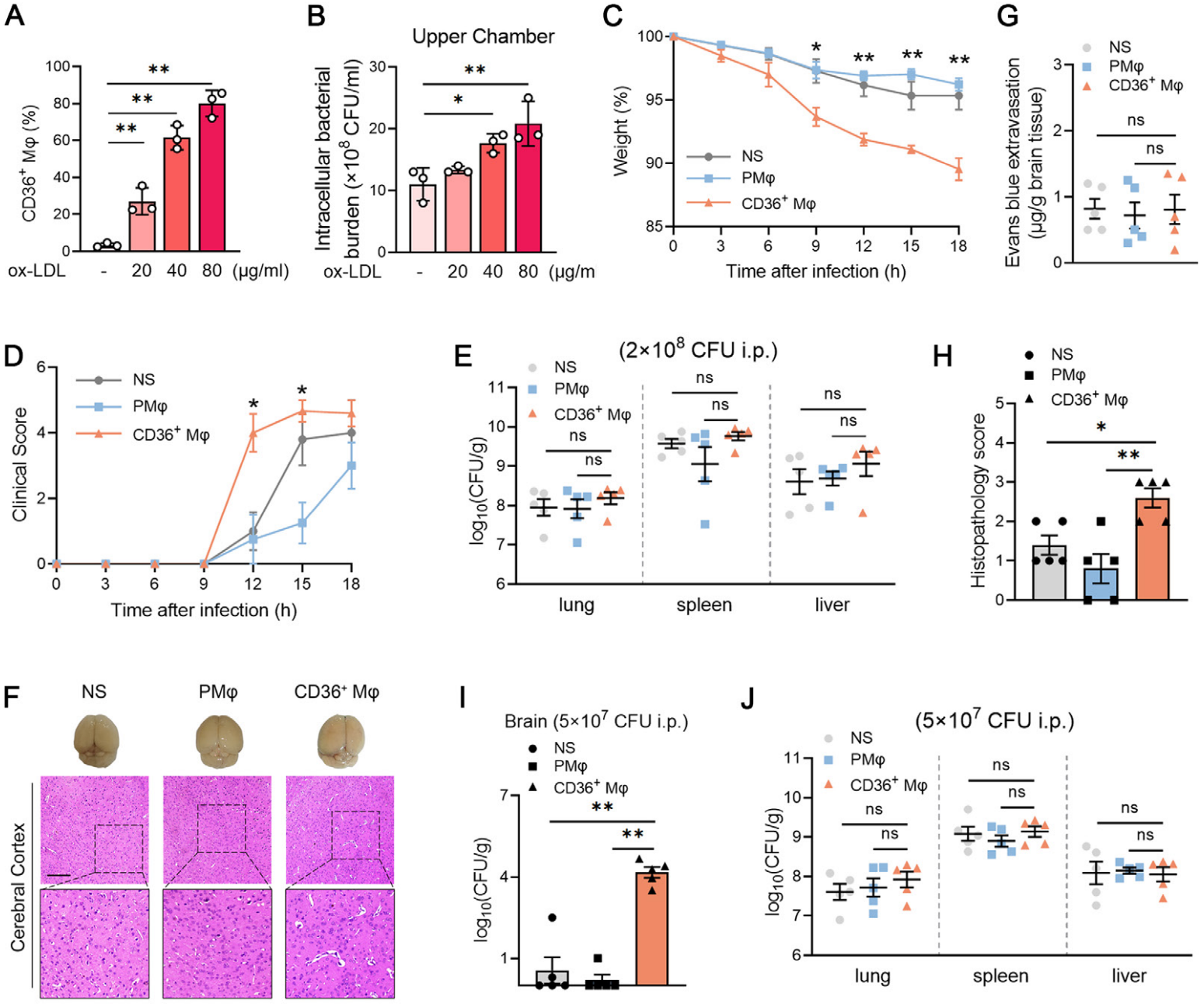

Supplementary Figure 2

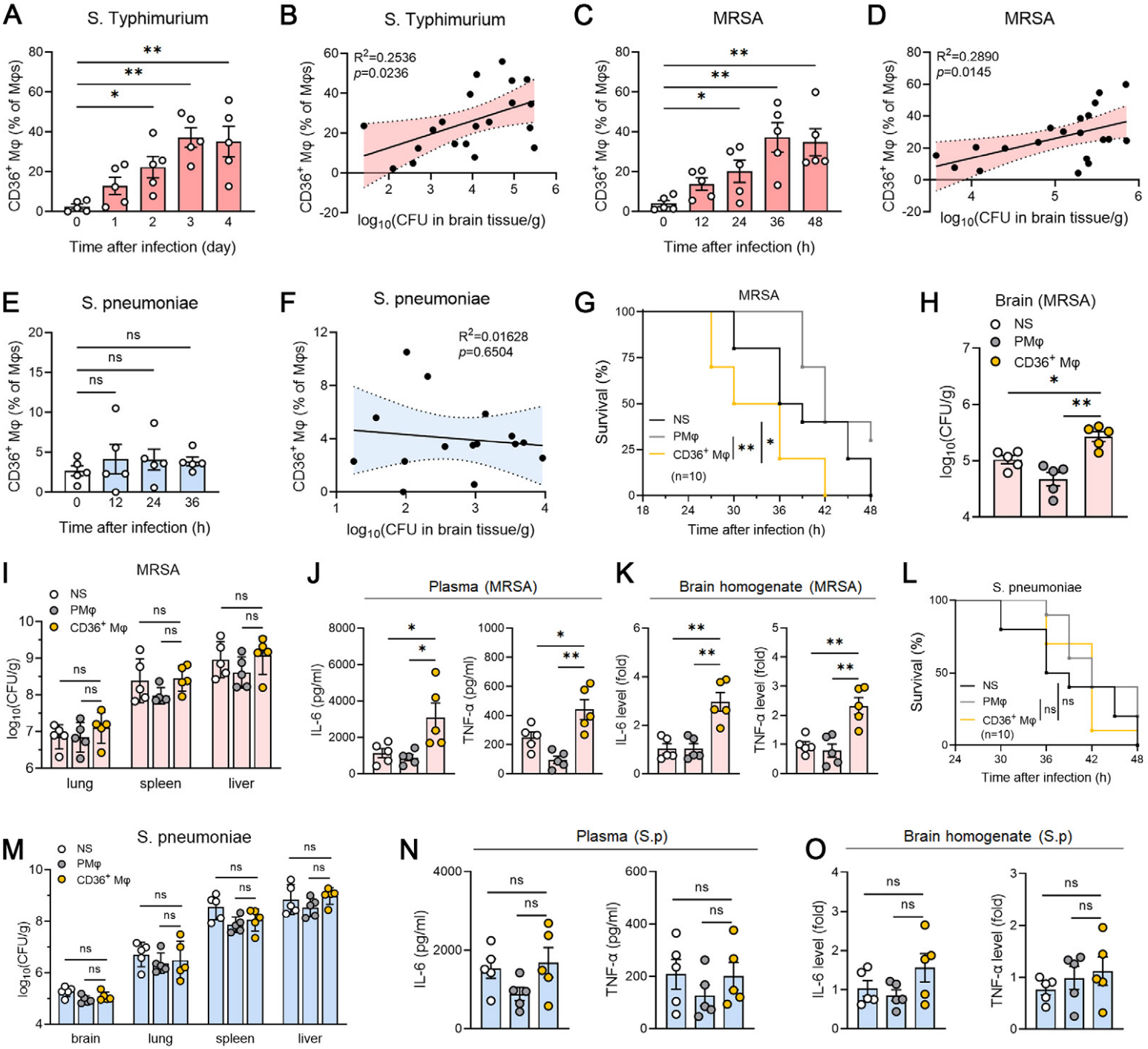

Supplementary Figure 3

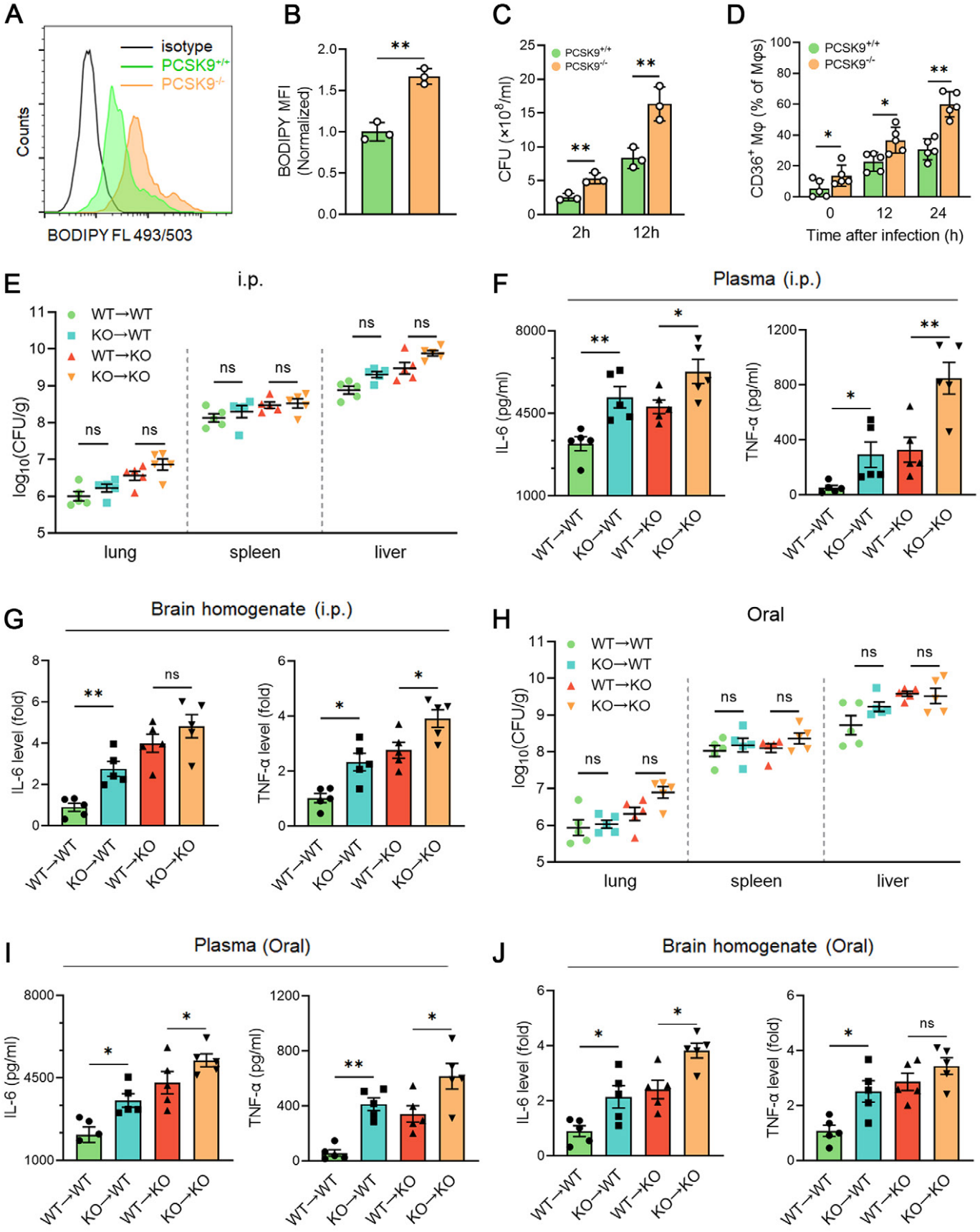

Supplementary Figure 4

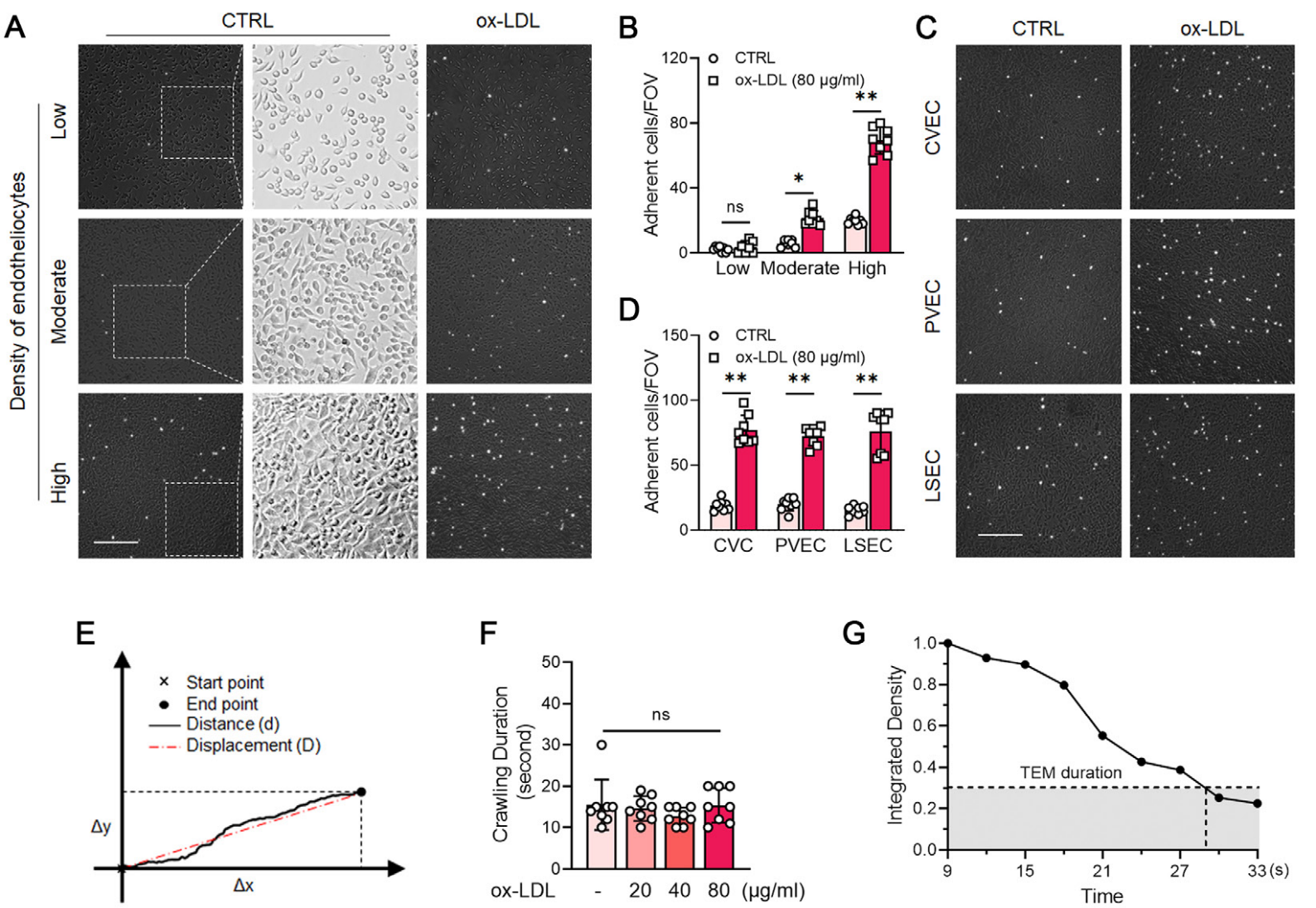

Supplementary Figure 5

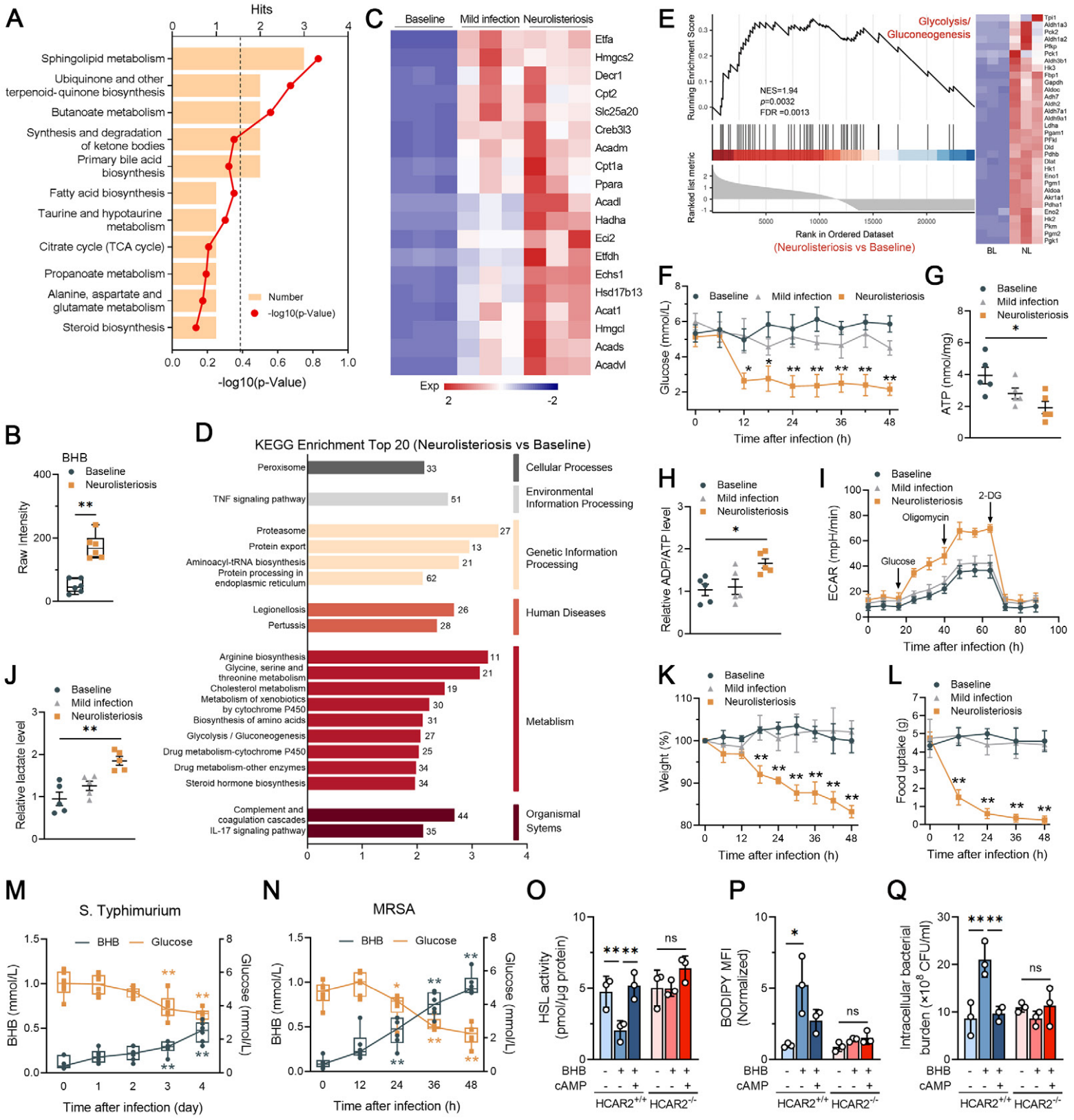

Supplementary Figure 6

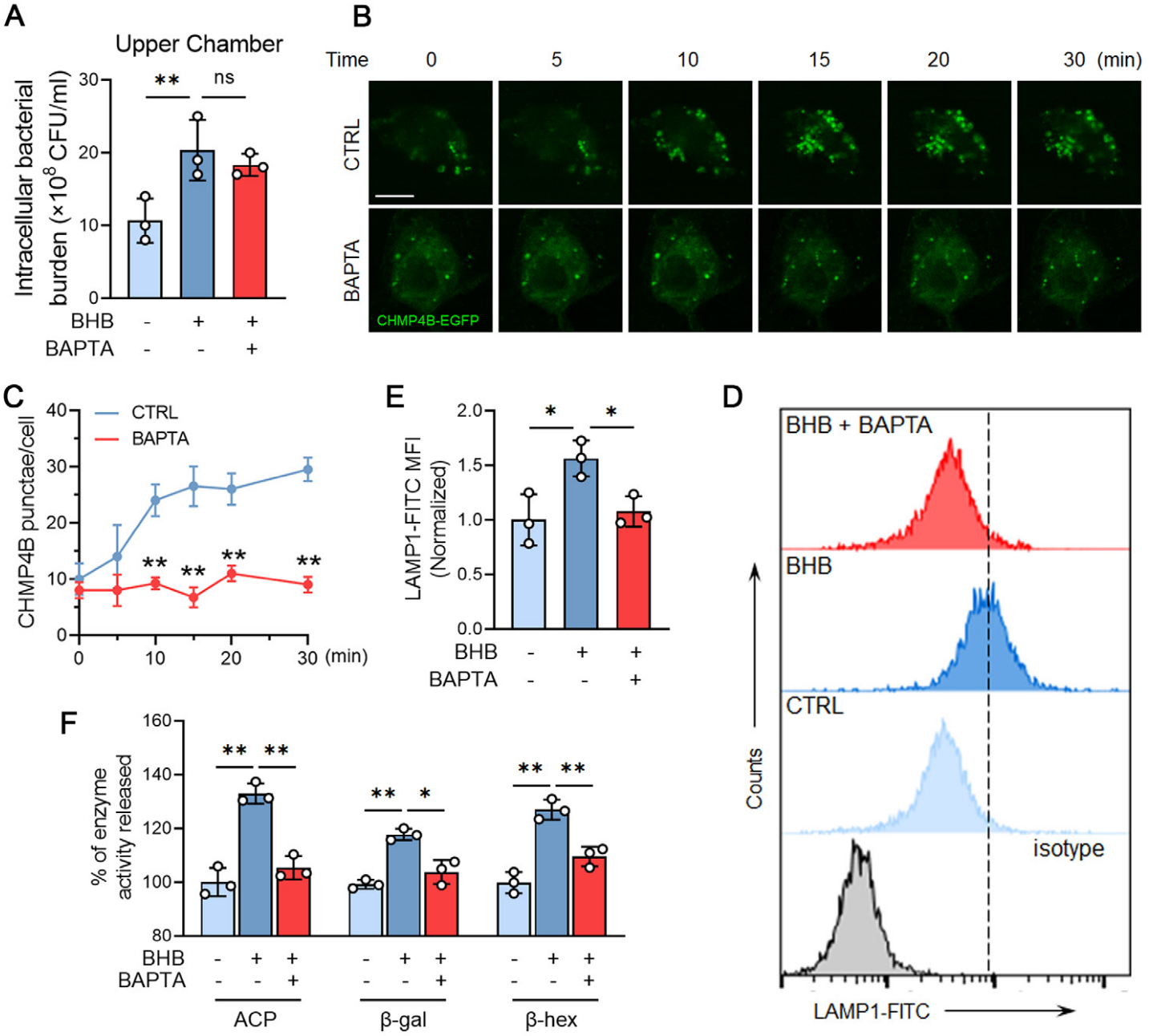

Supplementary Figure 7

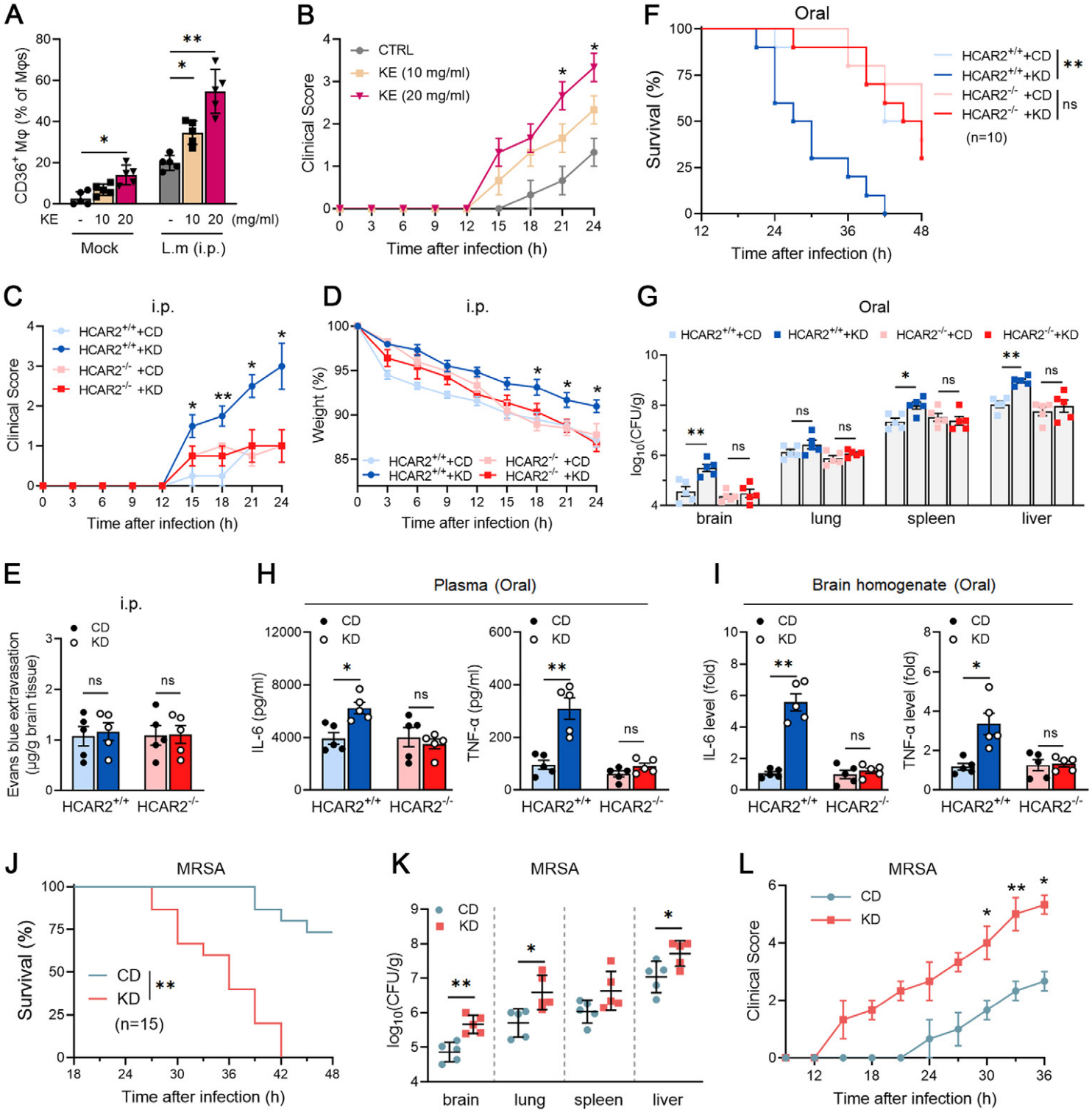

Supplementary Figure 8

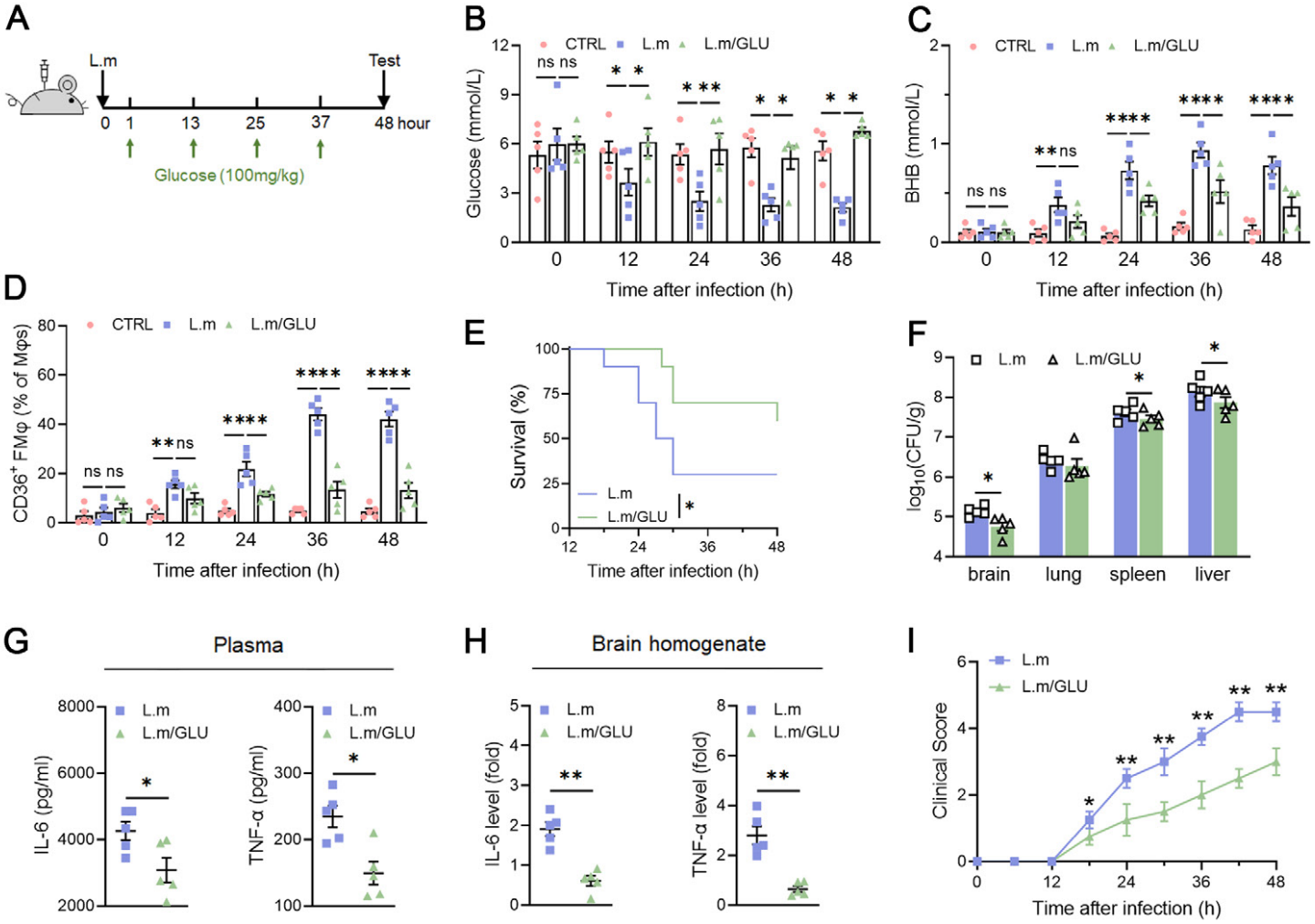

Supplementary Figure 9

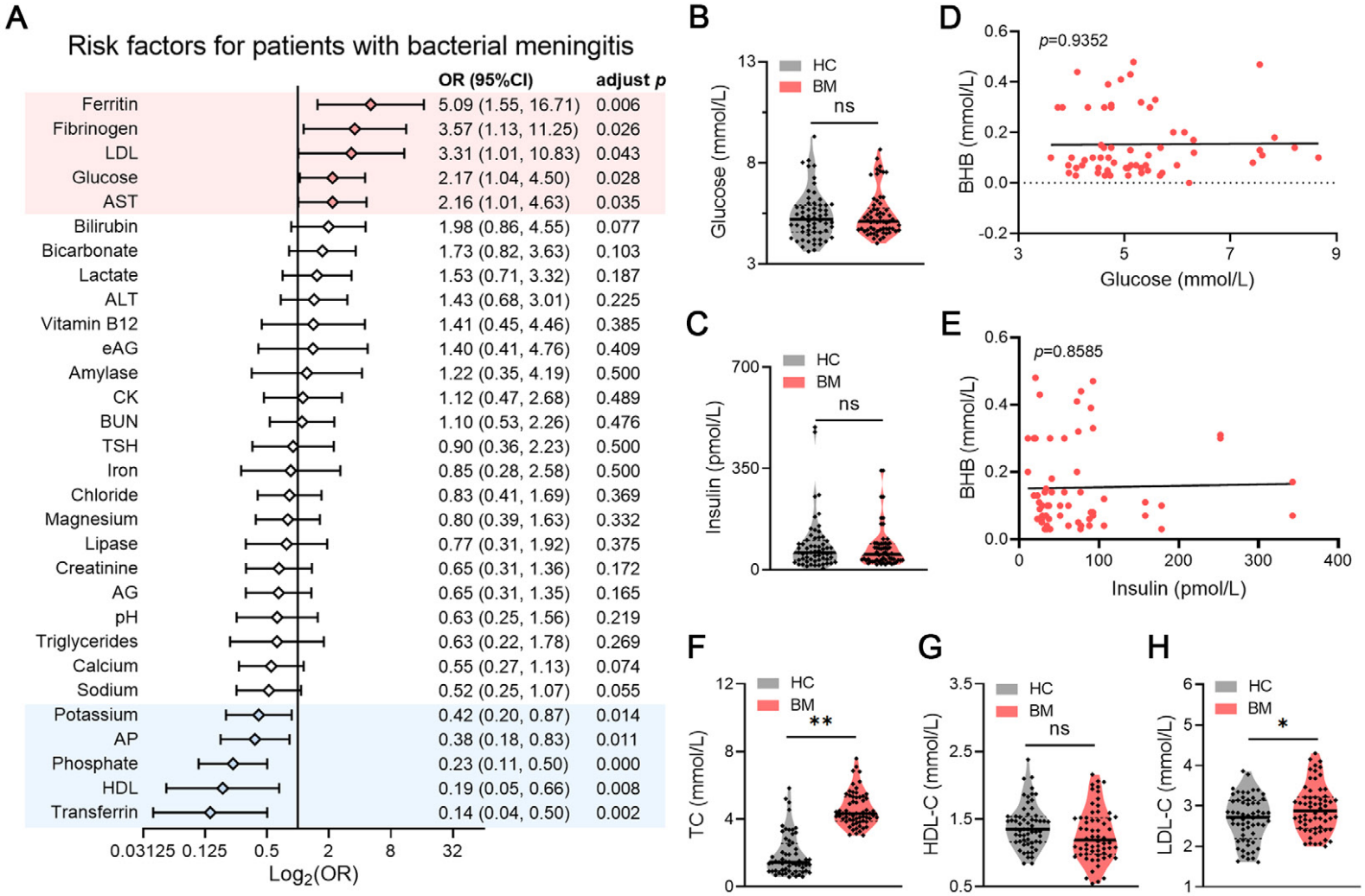

Supplementary Figure 10